Mechanical coupling coordinates microtubule growth

Bonnibelle K. Leeds, Katelyn F. Kostello, Yuna Y. Liu, Christian R. Nelson, Sue Biggins, and Charles L. Asbury

Abstract

During mitosis, kinetochore-attached microtubules form bundles (k-fibers) in which many filaments grow and shorten in near-perfect unison to align and segregate each chromosome. However, individual microtubules grow at intrinsically variable rates, which must be tightly regulated for a k-fiber to behave as a single unit. This exquisite coordination might be achieved biochemically, via selective binding of polymerases and depolymerases, or mechanically, because k-fiber microtubules are coupled through a shared load that influences their growth. Here, we use a novel dual laser trap assay to show that microtubule pairs growing *in vitro* are coordinated by mechanical coupling. Kinetic analyses show that microtubule growth is interrupted by stochastic, force-dependent pauses and indicate persistent heterogeneity in growth speed during non-pauses. A simple model incorporating both force-dependent pausing and persistent growth speed heterogeneity explains the measured coordination of microtubule pairs without any free fit parameters. Our findings illustrate how microtubule growth may be synchronized during mitosis and provide a basis for modeling k-fiber bundles with three or more microtubules, as found in many eukaryotes.

Introduction

In the mitotic spindles of many eukaryotes, each chromosome is attached to a bundle of microtubules (Kiewisz et al., 2022; McDonald et al., 1992; O'Toole et al., 2020; VandenBeldt et al., 2006) that grow and shorten in unison, acting as a single unit to produce the forces necessary to move the chromosome (Cimini et al., 2004). Microtubules are microns-long protein polymers composed of αβ-tubulin dimers with their 'minus' ends oriented toward the spindle poles and their more dynamic 'plus' ends oriented toward the chromosomes. Microtubule plus-ends, or tips, attach to chromosomes via protein complexes called kinetochores to form 'k-fiber' bundles. Kinetochore-attached tips within a single k-fiber remain very close to one another (within ~0.2 µm along the bundle axis) (O'Toole et al., 2020) even as the bundle grows and shortens (Cimini et al., 2004) by the addition and loss of tubulin subunits at each tip (Maddox et al., 2003). The number of microtubules per k-fiber varies across species; human RPE1 cells have ten to fifteen microtubules per k-fiber, while marsupial PTK2 cells have more than twenty, and cervid Indian Muntjac cells have up to sixty (O'Toole et al., 2020; Drpic et al., 2018). Budding yeast lack k-fiber bundles, having just a single microtubule per kinetochore (Winey et al., 1995), although microtubules attached to sister kinetochores on opposite sides of the yeast spindle must still coordinate with each other. Uncovering how microtubule tips maintain a high degree of synchrony

within k-fibers of up to sixty microtubules is critical to understanding how chromosomes are accurately segregated during normal mitosis and why even modest perturbations of kinetochore-attached microtubule dynamics can lead to mis-segregation (Bakhoum & Compton, 2012; Bakhoum et al., 2009; Ertych et al., 2014; Stumpff et al., 2014).

The tightly coordinated growth of microtubules within a k-fiber bundle is remarkable because individually, microtubule tips exhibit highly variable growth speeds and switch stochastically between distinct states of growth and shortening (Brouhard, 2015). Microtubule growth speed varies considerably in purified tubulin systems (Figure 1a) (Cleary et al., 2022; Gildersleeve et al., 1992; Mahserejian et al., 2022), in cell extracts (Geisterfer et al., 2020), and in live cells (Cassimeris et al., 1988; Gaudenz et al., 2010; Yamashita et al., 2015). Part of this heterogeneity can be attributed to pausing, when microtubules stochastically stop and start growing during periods of net growth (Amoah-Darko & White, 2022; Mahserejian et al., 2022). How the intrinsic heterogeneity of microtubule growth is coordinated to maintain sub-micrometer proximity between k-fiber tips remains a mystery.

One possible mechanism that might coordinate k-fiber microtubules is selective binding of microtubule-regulatory proteins (Maiato, Rieder, et al., 2003; McAinsh & Meraldi, 2011; Tirnauer et al., 2002). Many microtubule-associated proteins that are known to regulate growth *in vitro* are implicated in modulating k-fiber dynamics and kinetochore movements in cells, including TOG-family proteins such as XMAP215 (Brouhard et al., 2008) and CLASP (Al-Bassam et al., 2010; Maiato, Fairley, et al., 2003; Sousa et al., 2007), mitotic kinesins such as MCAK and Kif18A (Sanhaji et al., 2011; Stumpff et al., 2012), and other plus-end-trackers such as EB1 (reviewed in (Amin et al., 2019)). The localization of some of these regulators is enriched near kinetochores specifically when a kinetochore is moving anti-poleward and its k-fiber is growing longer (Amaro et al., 2010; Castrogiovanni et al., 2021; Tirnauer et al., 2002). However, whether such selective enrichment is sufficient to explain the very tight coordination across many individual microtubule tips within a k-fiber is unclear.

Another, simpler mechanism is suggested by the fact that microtubule dynamics are also strongly affected by mechanical force. Tension applied to individual microtubules *in vitro* biases them toward growth (Figure 1a) (Akiyoshi et al., 2010), while compression biases them toward shortening (Dogterom & Yurke, 1997; Janson et al., 2003). Theoretically, these mechanical effects should promote synchronization of any group of microtubules whose tips, like the tips of kinetochore-attached microtubules within a k-fiber, are all coupled to the same load (Banigan et al., 2015; Schwietert & Kierfeld, 2020; Skibbens et al., 1993). To illustrate how, consider a hypothetical k-fiber composed of just two microtubules sharing a total load, F_{TOT}. The load is transmitted to the microtubule tips through the kinetochore, which has elasticity (Cojoc et al., 2016; Renda et al., 2020) that we represent as spring-like connections from the kinetochore to each tip (Figure 1b). Initially, the two microtubules might have equal lengths and share the load equally – each one carrying half of F_{TOT} (Figure 1b, step 1). If one tip happens to grow more slowly than the other, then its spring will be stretched more, and it will start carrying more tension than the other tip (Figure 1b, step 2). Conversely, the faster-growing tip will start carrying less tension. Because tension accelerates microtubule growth, the lagging tip will tend to

accelerate, while the leading tip will tend to slow down, such that, on average, they return to having equal lengths and tensions (Figure 1b, step 3).

Mechanical coupling was proposed decades ago as an explanation for coordination between sister k-fibers (Gardner et al., 2005; Khodjakov et al., 1996; Skibbens et al., 1995; Skibbens et al., 1993; Wan et al., 2012), but how effectively it can coordinate microtubules within a k-fiber has not been determined. Compressive forces can cause a bundle of microtubules growing *in vitro* to switch cooperatively into a shortening state (Laan et al., 2008), but k-fiber bundles are usually under tension, not compression (Khodjakov & Rieder, 1996; Waters et al., 1996). Theoretical studies have explored the effects of shared tensile and compressive loads on cooperative switching and bi-stability in microtubule bundles (Banigan et al., 2015; Das et al., 2014; Ghanti & Chowdhury, 2015; Schwietert & Kierfeld, 2020; Zelinski & Kierfeld, 2013). However, these studies have generally neglected any differences in growth speed between microtubules and therefore cannot address how much variability exists, nor how such variability is suppressed. Furthermore, to our knowledge, the possibility that part of this variability (and suppression thereof) can be attributed to tension-dependent pausing during microtubule growth has not been explored.

Here, we use a novel dual laser trap assay to test directly how well a constant shared load can coordinate a pair of microtubules growing *in vitro*. We show that when microtubule pairs are mechanically coupled to a single load through a material of sufficient stiffness, their growth is tightly coordinated. By re-analyzing recordings of individual microtubules growing under constant force (from (Akiyoshi et al., 2010)) and examining their stochastic pausing kinetics, we show that pausing is suppressed by tension. We then develop a theoretical model, based on the measured behaviors of individual growing microtubules, to describe both the natural variability and force dependence of growth using no free fit parameters. Simulations based on this model fit the dual-trap data well. Altogether, this work illustrates how mechanical coupling may coordinate microtubule growth and provides a basis for modeling k-fibers of three or more microtubules under a shared load.

Results

Dual-trap assay to measure coordination between paired microtubules *in vitro*

To study how mechanical coupling affects microtubule growth, we developed a novel technique which we call the dual-trap assay (Figure 2). The dual-trap assay is based on our previously developed single-trap (force-clamp) assay (Akiyoshi et al., 2010; Miller et al., 2016; Sarangapani et al., 2013), in which dynamic microtubules are grown from stabilized seeds bound to a biotinylated coverslip. Using the single laser trap, we attach an individual bead decorated with isolated yeast kinetochores to the growing plus-end of a single microtubule. A computer then continuously measures the bead position and adjusts the trap to exert a precise, constant level of tension on the microtubule via the kinetochore-decorated bead. Under this persistent feedback-controlled tension, kinetochore-beads typically track with the microtubule tips even as the tips stochastically grow and shorten.

Our new dual-trap assay uses two separate laser trapping microscopes, located adjacent to one another in the same room and connected to a single computer. On each of the two instruments, we attach a kinetochore-decorated bead to a dynamic microtubule plus-end. The computer then simultaneously monitors and controls the forces on both microtubules. Rather than keeping the force constant on each microtubule, the computer adjusts the forces dynamically to simulate an elastic coupling of both plus-ends to a single shared load (Figure 2a). Thus far, we have simulated only purely elastic couplers, where both coupling springs are linear (Hookean) with stiffness, κ (Figure 2b). In the future, more complex coupling materials with viscoelasticity (Cojoc et al., 2016) or strain-stiffening (Schwietert et al., 2022; Volkov et al., 2018) could also be simulated.

To begin a dual-trap experiment, we first choose the spring stiffness, κ, and the total shared load, F_{TOT}, which are kept constant (Figure 2a, step 1). After a kinetochore-decorated bead is attached to a growing plus-end on each of the two instruments, feedback-control is initiated and the two plus-ends are arbitrarily considered to be parallel, with tips side-by-side (i.e., both at $x_1 = x_2 = 0$) and sharing the load equally ($F_1 = F_2 = ½·F_{TOT}$) (Figure 2a, step 2). Because microtubule growth is intrinsically variable, the two microtubules subsequently grow at different speeds (Figure 2a, step 3). The computer then dynamically monitors the bead positions (Figure 2a, step 4) and adjusts the forces, F_1 and F_2 (Figure 2a, step 5), according to the elastic coupling model (Figure 2b). For purely elastic couplers, the force difference across the two microtubules equals the tip separation, ($x_2 – x_1$), multiplied by the coupling stiffness (κ). When one microtubule grows more quickly than the other, tension on the leading (faster-growing) microtubule decreases and tension on the lagging (slower-growing) microtubule increases to maintain a constant total force on the pair, F_{TOT}. Forces in our dual-trap feedback system are updated at a rate of 50 Hz, which is more than sufficient for accurately simulating the elastic coupling between two microtubules (Figure S3-1). For all the experiments described below, F_{TOT} = 8 pN. Thus, each microtubule generally experiences between 1 and 7 pN of tension, close to the estimated average of 4 to 6 pN experienced by kinetochore-microtubules in budding yeast (Chacon et al., 2014; Parmar et al., 2023).

Mechanical coupling coordinates microtubule pairs *in vitro*

To measure the effects of mechanical coupling, we recorded the growth of many pairs of microtubules coupled to a constant shared load (F_{TOT} = 8 pN) either through relatively soft springs, with κ = 1 pN·µm^{-1}, or through springs with five-fold greater stiffness, κ = 5 pN·µm^{-1}. These two stiffnesses span a range near the minimum elasticities estimated for mitotic chromosomes (Nicklas, 1983; Poirier et al., 2002), for pericentromeres (Chacon et al., 2014), and for elements of the kinetochore (Schwietert et al., 2022; Volkov et al., 2018). When coupled through soft springs (κ = 1 pN·µm^{-1}), microtubule pairs tended to grow at different rates and their tips often became separated by more than a micrometer (Figure 3a, left, and Figure S3-1, left). After 300 s, the average tip separation for soft-coupled pairs grew to 0.8 ± 0.2 µm (mean ± SEM from N = 10 pairs) (Figure 3b, left). When coupled through stiff springs (κ = 5 pN·µm^{-1}), growth speeds were better matched, and the microtubule tips remained closer together

(Figure 3a, right, and Figure S3-1, right). The average tip separation for stiff-coupled pairs after 300 s was 0.25 ± 0.06 µm (mean ± SEM from N = 10 pairs) (Figure 3b, right), significantly lower than for soft-coupled pairs (p = 0.03 based on a Wilcoxon-Mann-Whitney two sample rank test).

Because the plus-ends of microtubules within k-fiber bundles are rarely separated by more than 0.8 µm from each other *in vivo* (O'Toole et al., 2020), we used Kaplan Meier survival analysis to ask how often the pairs of coupled microtubule tips in our experiments exceeded this threshold separation. Consistent with their lower average tip separation, stiff-coupled microtubule pairs were much less likely to exceed a separation of 0.8 µm than their soft-coupled counterparts (p = 0.01, log-rank test) (Figure 3c), which sometimes separated by 0.8 µm in as little as 60 s. Even after 400 s, more than 80% of the stiff-coupled pairs had tip separations that remained below 0.8 µm, while fewer than half of the soft-coupled pairs had tip separations below 0.8 µm. (Similar survival analyses using thresholds of 0.4, 0.6, and 1.2 µm are provided in Supplemental Figure S6-2.)

Even at shorter time periods, the average behavior of soft- and stiff-coupled microtubule pairs was distinct. During the first 100 s of growth, the average rate of tip separation for soft-coupled pairs was 0.23 ± 0.04 $\mu m \cdot min^{-1}$ (mean ± SEM from N = 23 pairs), while the average rate of tip separation for stiff-coupled pairs was only 0.14 ± 0.02 $\mu m \cdot min^{-1}$ (mean ± SEM from N = 26 pairs; p = 0.03 based on a Wilcoxon-Mann-Whitney two sample rank test). Notably, the average rate of tip separation for stiff-coupled microtubule pairs decreased as their average tip separation increased, suggesting they were approaching a steady-state level of separation (Figure 3b, right). In contrast, the average rate of tip separation for soft-coupled microtubule pairs remained approximately constant throughout the 400 s measurement, suggesting that soft-coupled pairs would require more time to approach a steady state. Altogether, these observations show that the growth of microtubule pairs can be tightly coordinated, even over relatively short (< 100 s) timescales, by mechanically coupling their tips to a shared load through couplers of sufficient stiffness.

Models of microtubule growth variability and force sensitivity can be derived from recordings of individual microtubules

Coordination of microtubule growth can be thought of as the suppression of variability in microtubule growth speed. Understanding how mechanical coupling suppresses this variability requires a realistic model of how the growth of individual microtubules varies over time and between microtubules, as well as how growth behaviors are influenced by force. Previous simulations of microtubule bundles (Banigan et al., 2015; Schwietert & Kierfeld, 2020), based on force-clamp measurements of individual microtubules (Akiyoshi et al., 2010), have suggested that mechanical coupling might coordinate the stochastic switching of microtubules between shortening and growth, such that sister k-fibers are nearly always kept in opposite states. However, these models assumed identical growth speeds for all microtubules under the same force, and therefore cannot address how mechanical coupling might coordinate differences in growth speed. We sought to create a model of

186 microtubule growth that explains both the variability in microtubule growth speeds and how that
187 variability is suppressed by sufficiently stiff mechanical coupling, as observed in the dual-trap assay.

188 To characterize the variability and force dependence of microtubule growth, we re-examined
189 the force-clamp recordings by Akiyoshi et al., 2010. This large dataset (N = 356 recordings) was recorded
190 with an identical setup to our dual-trap experiments, except that each microtubule was grown
191 individually with a single laser trap exerting a constant level of tension (between 0.5 and 18 pN). Using
192 this dataset, we created two models derived from the natural variability of individual kinetochore-
193 attached microtubules and their average behaviors as a function of force. Below, we begin by briefly
194 describing a simple non-pausing model, which was developed first and served as a foundation for our
195 second, more successful pausing model. The pausing model reasonably explains our dual-trap results by
196 incorporating both stochastic pausing and intrinsic differences in microtubule growth speed.

197

198 **A simple non-pausing model predicts larger tip separations than measured *in vitro***

199 When averaged across time and across many individual microtubules, mean growth speed
200 increases exponentially with applied tension (Akiyoshi et al., 2010), such that

201 $$v_g = v_o * exp\left(\frac{F}{F_g}\right) \qquad [1]$$

202 where v_o represents the unloaded growth speed, F represents the applied tension, and F_g represents
203 the sensitivity with which the growth speed increases with tension. However, individual microtubules
204 show considerable variability around this mean behavior, with some microtubules remaining
205 persistently slower than others for many minutes (Figure 1a). In our first model, we adopted the simple
206 assumptions that this variability stems entirely from intrinsic differences in unloaded microtubule
207 growth speed, v_o, and that all microtubules have identical force-sensitivity (with F_g = 8.4 pN, based on
208 the exponential curve that best fit the mean growth speed-vs-force data (Akiyoshi et al., 2010)). In
209 principle, such static heterogeneity in growth speed might arise from persistent differences in
210 microtubule tip structure (Cleary & Hancock, 2021; Mahserejian et al., 2022; Rai et al., 2021) or from
211 variation in the numbers of protofilaments per microtubule (Chretien et al., 1992; Rai et al., 2021).

212 For each simulated microtubule, we randomly chose an individual growth speed measurement
213 from the force-clamp dataset (Akiyoshi et al., 2010), then extrapolated the microtubule's intrinsic
214 unloaded speed (v_o) from the chosen point (v_g, F) using equation [1] with F_g = 8.4 pN. The growth
215 speed of this simulated microtubule then followed the extrapolated curve as a function of force. To
216 simulate a pair of coupled microtubules, we made two such random draws from the dataset, defining
217 two distinct exponential (v_g-versus-F) relations for the two microtubules. (Bundles of three or more
218 microtubules could be simulated in the same manner by making additional draws.) We used a simple
219 Monte Carlo-based method (Gardner & Odde, 2010) to simulate traces of tip position versus time for
220 the pair. As in our dual-trap experiments, the simulated tip pairs were coupled with either soft or stiff

221 elastic springs to a constant shared load, F_{TOT} = 8 pN. Both the variability and force-dependence of
222 growth in the model were derived directly from the experimental force-clamp data, with no adjustable
223 ('free') parameters.

224 Despite its direct derivation from force-clamp data, the non-pausing model could not explain the
225 behavior of microtubule pairs measured in the dual-trap assay (Figure 4). Simulated microtubule pairs
226 developed much larger tip separations than real microtubule pairs over time, implying that this model
227 overestimates real microtubule variability. The simulated microtubule pairs showed especially poor
228 agreement with real microtubule pairs under the stiff-coupled condition (Figure 4c, red curves),
229 indicating that the non-pausing model also does not capture the degree to which real microtubules are
230 coordinated by mechanical coupling.

231

232 **Microtubule growth is interrupted by stochastic, force-dependent pauses**

233 Our simple non-pausing model lacked a notable behavior exhibited by microtubules that could
234 influence their response to tension: Microtubule growth is frequently interrupted by stochastic pauses
235 of varying durations, both in cells (Gaudenz et al., 2010; Sousa et al., 2007) and in purified tubulin
236 systems (Mahserejian et al., 2022; Stumpff et al., 2012). Indeed, pauses recorded during our force-clamp
237 (Figures 1a and S4-1b) and dual-trap assays (Figures 3a and S3-1) were frequent and often lasted tens of
238 seconds. Presumably, these pauses occur because the configuration of the growing microtubule tip
239 fluctuates and sometimes becomes transiently refractory to the incorporation of new tubulin subunits
240 (Cleary & Hancock, 2021; Mahserejian et al., 2022). We hypothesized that entry and exit into the pause
241 state might be force-dependent processes, and that pausing might therefore be a key aspect of
242 microtubule force-sensitivity.

243 To test whether pause entry and exit rates vary with force, we reanalyzed the force-clamp
244 dataset (Akiyoshi et al., 2010), applying a 2 s sliding window to identify intervals during each recording
245 (N = 356) when the instantaneous growth speed fell to near-zero, indicative of a pause (Figure S5-1; see
246 Materials and Methods for details about our pause marking procedure). The intervals in-between these
247 pauses were designated as 'runs.' Distributions of run and pause durations were approximately
248 exponential (Figure S5-2), consistent with a relatively simple two-state kinetic model of microtubule
249 growth (Figure S5-1a), in which pause entry and exit are considered Poisson processes. For each force
250 level, we estimated the pause entry and exit rates, k_{EN} and k_{EX}, by counting the total number of
251 observed entrances into and exits out of pause and dividing by the total time spent in run and pause,
252 respectively (Figure S5-1a).

253 This analysis revealed that tension delays pause entry and accelerates pause exit (Figure 5a).
254 Both effects tend to decrease the time spent in the pause state for growing microtubule tips under high
255 tension. In addition, the average growth speed during runs was accelerated by tension (Figure 5b). All
256 three rates, pause entry, pause exit, and average growth speed during runs, were well-fit by single
257 exponential functions of force (Figure 5; see Table 1 for fit parameters). These observations show that

258 stochastic pausing during microtubule growth is force-dependent and imply that pausing kinetics will
259 strongly influence the response of growing microtubules to mechanical coupling.

260

261 **A pausing model can explain the variability between paired microtubule and their coordination by**
262 **mechanical coupling**

263 To examine how force-dependent pausing might affect the behavior of coupled microtubules,
264 we created a second model in which growing microtubules switch stochastically between states of
265 pause and run. Pause entry and exit were considered Poisson processes with kinetic rates dictated by
266 the exponential fits of k_{EX} and k_{EN} versus force estimated from the force-clamp dataset (Figure 5a,
267 dashed curves; Table 1). Intrinsic heterogeneity among microtubules was incorporated by randomly
268 choosing an individual run speed measurement for each simulated microtubule from the force-clamp
269 dataset (i.e., by randomly choosing one point in Figure 5b). We then extrapolated the microtubule's
270 intrinsic unloaded run speed (v_{RUN}^{o}) from the chosen point (v_{RUN}, F) by assuming an exponential force-
271 dependence with sensitivity F_{RUN} = 14.8 pN (based on the dashed curve in Figure 5b; Table 1). The
272 growth speed during runs for this simulated microtubule then followed the extrapolated curve as a
273 function of force. We used a simple Monte Carlo-based method (again) to simulate traces of
274 microtubule tip position versus time. All model parameters were derived directly from the experimental
275 force-clamp data, with no adjustable ('free') parameters. As in our dual-trap experiments, simulated
276 microtubule tip pairs were coupled with either soft or stiff elastic springs to a constant shared load, F_{TOT}
277 = 8 pN. Simulations of individual microtubules growing under constant force closely resembled force-
278 clamp recordings of real microtubules *in vitro*. (Compare Figure S6-1 to Figure 1a.)

279 The pausing model of microtubule growth provided significantly better fits to our dual-trap data
280 than the non-pausing model. Like real microtubules in the dual-trap experiments, the simulated pairs of
281 tips tended to drift apart under soft-coupled conditions, while under stiff-coupled conditions they
282 stayed closer together (Figure 6a). After 300 s, the average tip separation for simulated soft-coupled
283 pairs grew to 0.79 ± 0.01 µm (mean ± SEM from N = 10,000 simulations), while simulated stiff-coupled
284 pairs had a lower average tip separation of 0.43 ± 0.005 µm (mean ± SEM from N = 10,000 simulations)
285 (Figure 6b), similar to the corresponding separations measured in dual-trap experiments (0.8 ± 0.2 µm
286 and 0.25 ± 0.06 µm, respectively). Simulated pairs of microtubule tips under stiff-coupled conditions
287 were also less likely to exceed a threshold separation of 0.8 µm (Figure 6c, dashed curves), similar to the
288 survival analyses of microtubule pairs measured with the dual-trap assay (Figure 6c, solid curves).
289 (Survival analyses of simulated microtubule pairs with threshold separations of 0.4, 0.6, and 1.2 µm also
290 resembled the survival analyses of microtubule pairs measured with the dual-trap assay. See Figure S6-
291 2.) In addition, the pausing model scored better than the non-pausing model when we used probability
292 to compare simulated to *in vitro* measurements (Figure S6-4). (To quantify the variability due to
293 stochastic pausing alone, we also compared the pausing model to a version in which we assumed that
294 microtubules were intrinsically identical ('ergodic'). The low variability predicted by this model (Figure
295 S6-3), particularly under the soft-coupled condition, indicates that stochastic pausing alone is

insufficient to generate the large and persistent differences in growth speed exhibited by real microtubules). Overall, the strong agreement between the pausing model and the dual-trap recordings suggests that mechanical coupling coordinates microtubule growth in at least two distinct ways: first, by counteracting persistent (intrinsic) differences in microtubule growth speed, and second, by selectively suppressing stochastic pausing in the lagging tip relative to the leading tip.

Discussion

Our work demonstrates the effectiveness of mechanical coupling for coordinating the growth of microtubules and helps explain how numerous filaments within a k-fiber bundle can be tightly regulated to grow in near-perfect unison. Using our dual-trap assay, we found that pairs of microtubule tips growing *in vitro* are kept in close proximity when sharing a single load through a coupling material of sufficient stiffness. Tip pairs in our experiments were kept within a fraction of a micrometer by couplers of only κ = 5 pN·µm^{-1}, a modest stiffness within the ranges reported for elements of the kinetochore (Schwietert et al., 2022; Volkov et al., 2018), pericentromeric chromatin (Chacon et al., 2014), and mitotic chromosomes (Nicklas, 1983; Poirier et al., 2002). Because the kinetochore and its underlying centromeric chromatin both appear to deform together to maintain close contacts with k-fiber plus-ends *in vivo* (O'Toole et al., 2020), the plus-ends presumably exert forces on each other through a composite material composed of both kinetochore and chromatin. We propose that this mechanical coupling is a major coordinating influence on plus-end growth dynamics within k-fiber bundles.

Our dual-trap approach provides information that prior single-trap experiments, and theoretical work based solely on these prior measurements, cannot provide. Microtubules in real k-fiber bundles presumably adjust their growth speeds dynamically in response to the forces they exert on each other. The dual-trap assay uniquely allows this kind of mutual dynamic influence to be examined. Because each microtubule in the pair grows simultaneously in the same preparation of buffer, any differences in growth speed represent true biological variability, without the potentially confounding influences of prep-to-prep or sample-to-sample variability. While previous experiments with individual microtubules implied that a shared load should tend to coordinate growing microtubules, the dual-trap experiments are a direct, model-independent way to examine the extent to which load sharing can suppress the intrinsic variability of microtubules growing under identical conditions. With the dual-trap assay, we can test models and assumptions about microtubule tension-dependence and variability derived from recordings of individual microtubules, as we did with the pausing and non-pausing models presented here.

Since most known eukaryotes have k-fibers of more than two microtubules, an important area of future work will be to study how effectively mechanical coupling can coordinate k-fibers with more microtubules. While extending our *in vitro* laser trap methods to more than two microtubules is impractical, our model can be easily extended to explore mechanical coordination within k-fibers of three or more microtubules. Simulation parameters, such as microtubule growth speeds, can also be changed to explore how well mechanical coupling coordinates microtubules in different cell types or cell cycle stages with varying microtubule dynamics (Cassimeris et al., 1988; Gaudenz et al., 2010; Yamashita

335 et al., 2015; Rusan et al., 2001). Similarly, simulations can be used to study how the addition of
336 microtubule polymerases or depolymerases with known effects on microtubule dynamics influences
337 coordination.

338 A variety of microtubule-modifying proteins are implicated in regulating k-fiber dynamics (reviewed
339 in (Ou & Scholey, 2022) and (Amin et al., 2019)). These biochemical factors must work in concert with
340 mechanical effects, and we suggest that the two classes of mechanisms probably operate over different
341 length- and timescales. Certain tip-tracking proteins capable of influencing microtubule dynamics are
342 enriched at growing k-fiber ends specifically near kinetochores that are moving anti-poleward (Amaro et
343 al., 2010; Castrogiovanni et al., 2021; Tirnauer et al., 2002). Various kinesins are known to regulate the
344 size of the metaphase spindle (Goshima et al., 2005; Neahring et al., 2021), to influence k-fiber dynamics
345 (Maiato, Fairley, et al., 2003; Rizk et al., 2009; Stumpff et al., 2012; Wordeman et al., 2007), and to alter
346 microtubule dynamics *in vitro* in a length-dependent manner (Varga et al., 2006). However, it is unclear
347 whether the specific enrichment of such microtubule-modulators on longer or faster-growing tips could
348 occur quickly enough and with enough selectivity to slow the growth of a single tip that has grown
349 ahead of its neighbors by only a fraction of a micrometer, as required for tight coordination within a k-
350 fiber. On the other hand, mechanical forces would be transmitted essentially instantaneously between
351 neighboring tips through local deformations of the material through which the tips are coupled.
352 Therefore, mechanical coupling could account for the rapid, sub-micron responses required to
353 coordinate microtubule tips within a k-fiber, while microtubule-modifiers and spindle-wide phenomena,
354 like polar ejection forces and poleward flux, are likely to help set overall k-fiber length (Risteski et al.,
355 2021).

356 We found that tension accelerates microtubule growth not only by directly increasing growth speed,
357 but also by decreasing time spent in pause. More specifically, tension reduced the rate at which growing
358 tips entered a pause state. This finding implies that pause entry is associated with movement of tension-
359 bearing elements at the tip toward the minus end, opposite the direction of applied force and therefore
360 inhibited by the force. Tension also increased the rate at which paused tips resumed growth, which
361 implies that pause exit is associated with movement toward the plus-end, in the same direction as the
362 applied force and therefore assisted by the force. These tension-dependent dynamics may reflect
363 mechanical deformations of the microtubule tip; perhaps pauses occur when newly added tubulin
364 dimers at a growing tip adopt curved structures that disfavor lateral bonding (McIntosh et al., 2018).
365 Tension could help straighten these curved structures, thereby accelerating lateral bond formation and
366 favoring growth (Cleary & Hancock, 2021).

367 We derived a model of microtubule growth with no free parameters, based on constant-force
368 recordings of individual microtubules (from (Akiyoshi et al., 2010)), and found that a combination of
369 stochastic, force-dependent pausing and intrinsic differences in microtubule growth speed explained
370 both the variability and the coordination measured in our dual laser trap assay. The necessity of
371 including microtubules with different intrinsic growth speeds for our model's success implies structural
372 heterogeneity in the growing tips that must persist for many minutes, even as thousands of tubulin
373 subunits are being added. In principle, these persistent differences might arise from different or

374 mismatched protofilament numbers (Chretien et al., 1992; Rai et al., 2021) or the accumulation of other
375 lattice defects (Wieczorek et al., 2015) that result in varying degrees of tip taper (Coombes et al., 2013)
376 (or tip "raggedness" (Brouhard & Rice, 2018)) which are more or less conducive to microtubule growth.

377 For technical reasons, we focused exclusively here on microtubule tips in a state of net growth.
378 However, coordination of k-fiber microtubules *in vivo* presumably also requires tight regulation of tip
379 shortening speeds and rates of switching between growth and shortening (i.e., 'catastrophe' and
380 'rescue' rates) (Banigan et al., 2015; Schwietert & Kierfeld, 2020). These will be more difficult to study
381 with our dual-trap assay because switch events are stochastic and episodes of shortening are observed
382 less frequently than episodes of growth under our assay conditions. Nevertheless, the dual-trap
383 approach can be used in the future (potentially with a cutting laser to sever the microtubule tips to
384 induce shortening (Driver et al., 2017; Murray et al., 2022)) to study how mechanical coupling affects
385 microtubule pairs in which one or both filaments are shortening, as well as switch rates between
386 shortening and growth. Our dual-trap approach can also be adapted to examine mechanical coupling
387 through materials with complex mechanical properties, such as viscoelasticity and strain-stiffening
388 (Cojoc et al., 2016; Schwietert et al., 2022). In principle, the effect of mechanical coupling on pairs of
389 processive motor proteins (Holzbaur & Goldman, 2010) or on pairs of dynamic actin filaments linked to a
390 shared load (Garner & Theriot, 2022) can also be studied with the dual-trap approach. Overall, our work
391 demonstrates that mechanical coupling is a feasible mechanism that could coordinate k-fiber
392 microtubules and maintain their synchronous growth in the mitotic spindle.

393

394 **Funding and Acknowledgements**

395 We are grateful for feedback and critical reading of the manuscript from members of the
396 Biggins, Asbury, and Trisha Davis laboratories.

397 This work was supported by a Packard Fellowship 2006-30521 (to C.L. Asbury), National
398 Institutes of Health grants R01GM079373, P01GM105537, and R35GM134842 (to C.L. Asbury) and
399 R01GM064386 (to S. Biggins), and by the Genomics and Scientific Imaging and the Proteomics and
400 Metabolomics Shared Resources of the Fred Hutchinson/University of Washington Cancer Consortium
401 (P30 CA015704). S. Biggins is an investigator of the Howard Hughes Medical Institute. Research reported
402 in this publication was also supported by the National Institute of General Medical Sciences of the
403 National Institutes of Health under Award Number T32GM008268 (to B.K. Leeds).

404 Author contributions: Conceptualization (C.L. Asbury, B.K. Leeds), data curation (B.K. Leeds, Y. Liu),
405 formal analysis (B.K. Leeds, Y. Liu), funding acquisition (C.L. Asbury, S. Biggins, B.K. Leeds) investigation
406 (B.K. Leeds, K.F. Kostello, C.L. Asbury), project administration (C.L. Asbury), resources (C.L. Asbury, C.R.
407 Nelson, S. Biggins), software (B.K. Leeds, C.L. Asbury, Y. Liu), supervision (C.L. Asbury, S. Biggins, B.K.
408 Leeds), validation (B.K. Leeds, K.F. Kostello, Y. Liu, C.L. Asbury), visualization (B.K. Leeds, C.L. Asbury, K.F.
409 Kostello, Y. Liu), writing–original draft (B.K. Leeds, C.L. Asbury), writing–review and editing (B.K. Leeds,
410 C.L Asbury, K.F. Kostello, S. Biggins).

411

412 **Methods**

413 **Spring-coupler model**

414 For both *in vitro* and *in silico* experiments, the force on each microtubule plus-end was dictated
415 by a model in which plus-ends were coupled to a shared "kinetochore" via simple Hookean springs of
416 identical stiffnesses (Figure 2b). Because k-fibers grow relatively slowly in cells (Khodjakov et al., 1996;
417 Skibbens et al., 1993; Stumpff et al., 2012), we neglect viscous drag such that the sum of the forces on
418 individual k-fiber tips equals F_{TOT}. Microtubule pairs were considered to grow along a shared 1D axis.
419 Microtubules were assumed to be incompressible because microtubules have high axial stiffness
420 (Howard, 2001; Kis et al., 2002; Pampaloni et al., 2006) and are cross-linked in bundles (O'Toole et al.,
421 2020), thus forming the structural support required to maintain mitotic spindle integrity. Microtubules
422 were considered stationary except at the plus-end, so that only growth or shortening at the plus-end
423 affected plus-end position.

424

425 **Kinetochore purification**

426 Native kinetochore particles were purified from asynchronously grown *S. cerevisiae* SBY8253
427 cells (Genotype: MATa DSN1-6His-3Flag:URA3) grown in YPD medium (2% glucose) by modifying
428 previous protocols (Akiyoshi et al., 2010; Miller et al., 2016). Protein lysates were prepared using a
429 Freezer Mill (SPEX SamplePrep) submerged in liquid nitrogen. Lysed cells were resuspended in buffer H
430 (25 mM Hepes, pH 8.0, 2 mM MgCl2, 0.1 mM EDTA, 0.5 mM EGTA, 0.1% NP-40, 15% glycerol, and 150
431 mM KCl) containing phosphatase inhibitors (0.1 mM Na-orthovanadate, 0.2 µM microcystin, 2 mM β-
432 glycerophosphate, 1 mM Na pyrophosphate, and 5 mM NaF) and protease inhibitors (20 µg/ml
433 leupeptin, 20 µg/ml pepstatin A, 20 µg/ml chymostatin, and 200 µM PMSF). Lysates were
434 ultracentrifuged at 98,500 g for 90 min at 4°C. Protein G Dynabeads (Invitrogen) were conjugated with
435 an α-FLAG antibody (Sigma-Aldrich), and immunoprecipitation of Dsn1-6His-3Flag was performed at 4°C
436 for 3 h. Beads were washed once with lysis buffer containing 2 mM DTT and protease inhibitors, three
437 times with lysis buffer with protease inhibitors, and once in lysis buffer without inhibitors, and
438 kinetochore particles were eluted by gentle agitation of beads in elution buffer (buffer H + 0.5 mg/ml
439 3FLAG Peptide [Sigma-Aldrich]) for 30 min at room temperature.

440

441 **Bead functionalization and slide preparation for laser trap experiments**

442 To functionalize laser trapping beads with native kinetochore particles, streptavidin-coated
443 polystyrene beads (0.44 µm in diameter, Spherotech) were incubated with biotinylated anti-5His
444 antibodies (Qiagen) and stored for up to 6 months with continuous rotation at 4°C in BRB80 (80 mM
445 Pipes, 1 mM $MgCl_2$, and 1 mM EGTA, pH 6.9) supplemented with 8 $mg{\cdot}mL^{-1}$ bovine serum albumin and 1
446 mM DTT. Before each experiment, functionalized beads were sonicated for two minutes and decorated
447 with kinetochore particles by incubating 6 pM anti-5His beads for 1-2 hours at 4°C with purified

448 kinetochore material, corresponding to concentrations of Dsn1-His-Flag between 1.5 and 4 nM, well
449 within the single-kinetochore-particle condition described in (Akiyoshi et al., 2010).

450 Each flow chamber (~5-10 µL in volume) was constructed by placing two parallel strips of
451 double-stick tape between a glass slide and a KOH- or plasma-cleaned coverslip. Immediately before
452 every experiment, two flow chambers were each functionalized as follows. First, flow chambers were
453 incubated with 10 µL of 10 mg·mL^{-1} biotinylated bovine serum albumin (Vector Laboratories) for 15
454 minutes at room temperature. Chambers were then washed with 100 µL BRB80. Next, 20 µL of 333
455 mg·mL^{-1} avidin DN (Vector Laboratories) in BRB80 was added to the chamber and incubated for 3
456 minutes before washing again with 100 µL BRB80. Chambers were then incubated for 5 minutes with
457 GMPCPP-stabilized biotinylated microtubule seeds warmed for 5-10 minutes in BRB80. Next, chambers
458 were washed with 100 µL of growth buffer (1 mM GTP, 1 mg·mL^{-1} β-casein, and 0.08 mg·mL^{-1}
459 biotinylated bovine serum albumin in BRB80). Finally, chambers were incubated with kinetochore-
460 decorated beads diluted approximately 8-fold into growth buffer augmented with 1.5 mg·mL^{-1} purified
461 bovine brain tubulin and an oxygen scavenging system (1 mM DTT, 500 µg·mL^{-1} glucose oxidase, 60
462 µg·mL^{-1} catalase, and 25 mM glucose). The flow chamber exit and entrance were then sealed with nail
463 polish and used for experiments at 23°C for up to 2 hours.

464

465 **Performing the dual-trap assay**

466 Laser trap experiments were performed using two custom-built instruments based on
467 commercial inverted microscopes (Nikon; TE2000U) modified to each incorporate a trapping laser
468 (Spectra-Physics; J20I-BL-106C-NSI), a computer-controlled piezo specimen stage (Physik Instrumente; P-
469 517.3CL), and a position-sensitive photodetector (Pacific Silicon Sensor; DL100-7-PCBA2). Experiments
470 were performed at 22° C with a trap stiffnesses of 0.35 – 0.91 pN·nm^{-1}. See (Franck et al., 2010) for
471 details regarding instrument setup and calibration.

472 The dual-trap assay was modified from previous force-clamp protocols (Akiyoshi et al., 2010;
473 Franck et al., 2010; Miller et al., 2016) and maintained constant total force on two bead-laser trap
474 systems, rather than one (Figure 2a). Both lasers were controlled by a single computer, which adjusted
475 the force on each bead to maintain force equilibrium on the modeled coupler given the measured bead
476 positions (Figure 2b). The bead positions served as accurate proxies for the microtubule tip positions,
477 because kinetochore-decorated beads are known to track with microtubule plus-ends under tensions
478 between 0.5 and 18 pN (Akiyoshi et al., 2010; Asbury et al., 2006; Franck et al., 2010; Miller et al., 2016;
479 Powers et al., 2009; Tien et al., 2010). In addition, the yeast kinetochores used to link the beads to the
480 microtubule tips are very small, only ~130 nm in length (Gonen et al., 2012), compared to the relevant
481 micrometer-scale tip displacements. The small size of the yeast kinetochore, as well as the slow change
482 in force on each tip (Figure S3-1), ensures that the kinetochore's (visco)elastic properties did not
483 significantly affect experimental results, because any force-dependent changes in its length had a
484 negligible effect compared to tip growth.

485 To calibrate the laser trap's zero-force position, we recorded the position of a free bead using
486 each laser-trap at the start of each 2-hour experiment, and as necessary between recordings. Feedback
487 to exert precisely the amount of force dictated by the relative bead positions and the spring-coupler

488 model was implemented with custom LabView software (National Instruments). Bead-trap separation
489 was sampled at 40 kHz, while stage position to maintain the desired bead-trap separation (and thus
490 force) was updated at 50 Hz. Bead and stage position data were decimated to 200 Hz before storing to
491 disk, a temporal frequency which is more than sufficient to capture pauses and runs of many seconds.

492 LabView software to perform force-clamp experiments is available at
493 https://github.com/casbury69/laser-trap-control-and-data-acquisition and the LabView software to
494 perform dual-trap experiments is available at https://github.com/casbury69/dual-trap-control-and-data-
495 acquisition.

496

497 **Analyzing dual-trap recordings**

498 We analyzed recordings from the dual-trap assay using custom software made in Igor Pro 9
499 (Wavemetrics). First, by hand, we marked the beginning and end of recorded segments in which both
500 microtubules were growing and separated these episodes into individual recordings. We then calculated
501 the tip separation between coupled microtubules for each excised recording by taking the absolute
502 value of the difference in position at 1 s intervals from 0 to 400 s. For each recording, total force on the
503 microtubule pair was computed by adding the force on both microtubules together at 0.005 s intervals
504 (Fig. S3-1).

505 To calculate the speed of tip separation, we fit the first 100 s to a line with the Levenberg-
506 Marquardt method. Uncertainties in tip separation speed were estimated from residuals as described in
507 (Press et al.).

508 SEMs for microtubule pair tip separation measured using the dual-trap assay (Figure 3b) were
509 calculated at 1 s intervals after the recording began using the following equation:

$$SEM_{tip\ sep}(t) = \frac{\sigma_t}{\sqrt{N_t}}$$

510 where σ_t is the standard deviation of the tip separations at t seconds and N_t is the number of
511 microtubule pairs which were still growing and tip-attached to a bead at t seconds.

512 Download files at https://doi.org/10.5061/dryad.xksn02vnb to view position- and force-versus-
513 time curves for each of the dual-trap recordings analyzed in this work. See also 'Dual-trap anlaysis.txt' at
514 https://doi.org/10.5281/zenodo.8433109 for the software used to analyze dual-trap recordings.

515

516 **Creating Kaplan-Meier survival curves**

517 Kaplan-Meier survival curves for both simulated and *in vitro* microtubule pairs (Figure 3c, Figure
518 4c, Figure 6c, Figure S6-2, and Figure S6-3c) were calculated at 1 s intervals after the recording began
519 using the following equation:

$$S(t) = \prod_{j=0}^{t} \frac{n_j - d_j}{n_j}$$

where $S(t)$ is the Kaplan-Meier survival probability at t seconds, t is the number of Kaplan-Meier estimates made between time 0 and t seconds, n_j is the number of microtubule pairs still growing, tip-attached to a bead, and within the threshold tip separation at j seconds, and d_j is the number of microtubule pairs that exceeded the threshold tip separation (0.4, 0.6, 0.8, or 1.2 µm) between time $j-1$ and j seconds.

SEMs for Kaplan-Meier survival plots estimated using the dual-trap assay (Figure 3c and Figure S6-2) were calculated at 1 s intervals after the recording began using the following equation:

$$SEM_{survival}(t) = S(t) * \sqrt{\sum_{j=1}^{t} \frac{d_j}{n_j(n_j - d_j)}}$$

where $S(t)$ is the Kaplan-Meier survival probability at t seconds, t is the number of Kaplan-Meier estimates made between time 0 and t seconds, d_j is the number of microtubule pairs that exceeded the threshold tip separation (0.4, 0.6, 0.8, or 1.2 µm) between time $j-1$ and j seconds, and n_j is the number of microtubule pairs still growing, tip-attached to a bead, and within the threshold tip separation at j seconds.

Segmenting constant force traces into periods of run and pause

To estimate pause entrance and exit rates as a function of force, we segmented N = 356 recordings of growing microtubules under constant force (from (Akiyoshi et al., 2010)) into pauses and fast growth ('runs,' Figure S5-1a and b). First, we estimated the instantaneous growth speed over the entirety of each recording to be the slope of the best fit line for a sliding 2 s window (Figure S5-1c). Next, we defined a unique threshold between pause and run for each recording by assembling a histogram of growth speeds throughout the recording and fitting that histogram with a sum of between two and six Gaussian peaks. We centered one Gaussian at or near 0 µm·min^{-1} and defined it as the 'pause' peak. Fitting the growth speed histograms to Gaussian peaks was performed using the 'Multipeak fitting' package in Igor Pro 9. The intersection of the pause peak and the Gaussian with the next highest mean growth speed was identified for each individual recording and defined as the threshold to distinguish pauses and runs for that recording.

To reduce the impact of high-frequency noise, we excluded pauses and runs that lasted less than 1 s. If the instantaneous growth speed fell below that recording's predefined threshold for at least 1 s, the microtubule was considered to have paused. If the instantaneous growth speed fell below the threshold for less than 1 s, the short interval was combined with the run intervals before and after to make a single run. Likewise, if the instantaneous growth speed exceeded the threshold for at least 1 s, the microtubule was considered to be in run. If the instantaneous growth speed exceeded the threshold

551 for less than 1 s, the short interval was combined with the pause intervals before and after to make a
552 single pause. If the defined threshold was never crossed, the recording was considered a single run
553 interval.

554 The overall trends of tension suppressing pause entrance and promoting pause exit were
555 maintained irrespective of our choices of minimum event duration and smoothing window size. While
556 the 1 s minimum event duration decreased the overall frequency of pause entrances and exits, it did not
557 significantly affect the measured force sensitivities of pause entrance (F_{EN}) and exit (F_{EX}). Re-analyzing
558 the constant force recordings with only a 0.01 s minimum event duration, we measured force
559 sensitivities of F_{EN} = -5.1 pN and F_{EX} = 14.3 pN, compared to F_{EN} = -4.6 pN and F_{EX} = 14.1 pN with
560 the 1 s minimum event duration. The size of the smoothing window had a significant effect on measured
561 pause exit force sensitivity, but not pause entrance force sensitivity—re-analyzing the constant force
562 recordings with a 5 s smoothing window, we measured force sensitivities of F_{EN} = -4.4 pN and
563 F_{EX} = 24.8 pN. Ultimately, we chose the 2 s smoothing window and 1 s minimum duration threshold
564 because these choices resulted in recording segmentation that agreed best with how we would
565 differentiate pauses and runs by eye.

566 Download files at https://doi.org/10.5061/dryad.6djh9w16v to view position- and velocity-
567 versus time curves for each force-clamp recording analyzed in this work, as well as how pauses were
568 marked for each recording. This file also includes additional shortening events which were not studied
569 here. See also 'Force-clamp viewer.txt' at https://doi.org/10.5281/zenodo.8433062 for the software
570 used to distinguish pauses from runs.

571

572 **Quantifying growth speed during runs for individual recordings**

573 For each pause-based model that we considered, microtubule growth speed during runs was
574 assumed to be time-invariant under constant force. Thus, we made the same assumption when we
575 quantified the growth speed during runs of individual microtubules *in vitro*, and calculated a unique
576 growth speed during runs for each recording (dots in Figure 5b). The growth speed during each run
577 interval was calculated by averaging together the instantaneous growth speeds comprising that interval,
578 measured with the 2 s sliding window described above. We calculated the overall growth speed during
579 runs for a single microtubule by averaging together the growth speed of all contained run intervals,
580 weighted by the duration of that interval, such that:

$$v_{run} = \frac{\sum v_i * t_i}{T}$$

581 where v_{run} is the overall growth speed during runs for a particular recording, v_i is the growth speed for
582 the ith run interval, t_i is the duration of the ith run interval, and T is the total time spent in the run state.

583

584 **Quantifying the force dependence of pause entrance rates, exit rates and growth speed**

To calculate average pause exit rates, entrance rates, and growth speeds as a function of force we binned each recording by the constant tensile force to which the microtubule was subjected (Figure 5). For consistency, we used the same seven force bins used by (Akiyoshi et al., 2010) (see Table 2 for bin boundaries). For both the pause entrance and exit rate, we excluded the highest force bin from our analysis because of low statistics. For each force bin, we calculated the mean pause entrance and exit rate by counting the number of times microtubules in that force bin entered and exited pause and dividing by the total time microtubules in that bin spent in run and pause, respectively (Figure S5-1a). Error bars in the y-direction represent counting uncertainties, calculated with the equation:

$$SEM_{rate}(i) = \frac{k_i}{\sqrt{N_i}}$$

where k_i is the rate of pause entrance or exit for the ith force bin, and N_i is the number of pause entrances or exits in the recordings in the ith bin (N = 387 to 3502 pause entrances and N = 378 to 3501 pause exits per bin, see Table 2 for the number of pause entrances and exits by bin). Error bars in the x-direction represent standard deviations of forces for the recordings in each bin.

We found the mean growth speed during runs for each force bin by averaging together the growth speed during runs for all the recordings in that bin. Error bars in the y-direction represent the SEMs of growth speeds, calculated with the equation:

$$SEM_{run\ speed}(i) = \frac{\sigma_i}{\sqrt{N_i}}$$

where σ_i is the standard deviation of the growth speeds during runs, averaged over each recording, for the ith force bin, and N_i is the number of recordings in the ith bin (N = 9 to 85 recordings per bin, see Table 2 for the number of recordings by bin). Once again, error bars in the x-direction represent the standard deviations of forces for the recordings in each bin. Fit lines for pause exit and entrance rates and growth speed were calculated with Levenberg-Marquardt least-squares method (Press et al.).

Simulating pairs of growing microtubules

Simulated recordings using each model followed the same general procedure. For simulations in which the growth or run speed was different between microtubules (both non-ergodic models), the 'unloaded' growth or run speed was drawn from a distribution of measured growth or run speeds as described in the results section. For the non-ergodic pausing model, intrinsic unloaded run speeds ($v_{intrinsic}$) of more than 30 nm/s were considered outliers and excluded from the distribution. For microtubules simulated with the ergodic pausing model, both microtubules had the same growth speed during runs, based on the equation and parameters for v_{run} in Table 1. Each simulation began with both microtubules growing (in run, for pause-based models) from the same position under the same tensile force. As microtubules stochastically grew or paused, the tensile force on each microtubule evolved according to the spring-coupler model, just like they did in the dual-trap assay. As the force changed, depending on the model type, the growth or run speed changed according to exponential relationships with force estimated from (Akiyoshi et al., 2010) (Table 1).

619 A modified Gillespie algorithm was used to implement stochastic microtubule events: pause
620 entrance and exit, detachment from the kinetochore, switches into shortening (catastrophe), and other
621 event interruptions. Each of these event rates were assumed independent Poisson processes and were
622 derived directly from the data summarized in (Akiyoshi et al., 2010). Each microtubule was assumed to
623 have identical rates for all stochastic events, given the same external force. Detachment and
624 catastrophe rates were calculated using the exponential relationships as a function of force estimated
625 by (Akiyoshi et al., 2010).The rate of interruption by other events was also estimated from these force-
626 clamp recordings but was force-independent. For simulations that included pausing, rates of pause
627 entrance and exit were calculated from the fit equations in Table 1 (fit lines in Figure 5).

628 Because detachment, catastrophe, and pause rates are force-dependent, they can only be
629 approximated as Poisson (time-invariant) rates for short time intervals over which the force on the tip is
630 relatively constant. Consequently, we imposed a maximum timestep of no greater than 1 s for each
631 simulation. If the timestep chosen by our Gillespie algorithm exceeded the maximum timestep, no event
632 occurred and the microtubule continued growing during that 1 s interval. All simulations were
633 performed using custom software in Igor Pro 9 (Wavemetrics).

634 Download 'Dual-trap simulations.pxp' at https://github.com/casbury69/simulations-of-coupled-
635 microtubules to run dual-trap simulations as described in the results and see 'Dual-trap simulator.txt' at
636 https://github.com/casbury69/simulations-of-coupled-microtubules for the code used to run these
637 simulations.

638

639 **Comparing pausing and non-pausing models with simple probability**

640 To evaluate whether the pausing or non-pausing model was more likely given our dual-trap
641 measurements, we compared histograms of tip separations at 100 and 200 s after the start of the
642 recording or simulation (Figure S6-4). We used 0.1 µm bins for both simulated and dual-trap data and
643 normalized all histograms to have an area of 1.

644 We calculated the likelihood that simulations performed using the pausing and non-pausing
645 models would produce each *in vitro* tip separation:

$$L_{measurement} = w_{bin} * P_{normalized}$$

646 where w_{bin} is the bin width of the tip separation histogram (0.1 µm) and $P_{normalized}$ is the normalized
647 probability of the given model at the measured tip separation (y-values of the dashed lines in Figure S6-
648 4).

649 To compare the overall likelihood that the pausing and non-pausing simulations would produce
650 all the tip separations measured *in vitro*, we multiplied together the likelihoods of each measurement
651 for a given model at a given coupler stiffness and at a given time point. We calculated the log likelihood
652 by taking the base 10 logarithm of each probability (reported in the right-hand column of each table in
653 Figure S6-4).

654

655 **Statistical analysis**

656 All statistical analysis was performed using custom software written in Igor Pro 9 (Wavemetrics).

657 We calculated p-values to determine whether survival curves of stiff-coupled and soft-coupled
658 *in vitro* microtubule pairs were statistically different for each threshold tip separation using a log-rank
659 test. For each survival curve, at 1 s intervals after the recording began, we calculated an expected value
660 using the following equation:

$$E(t) = \frac{n_t}{n_{tot}}(d_{tot})$$

661 where n_t is the number of microtubule pairs comprising one survival curve that are still growing, tip-
662 attached to a bead, and within the threshold tip separation at t seconds, n_{tot} is the total number of
663 microtubule pairs comprising both survival curves being compared that are still growing, tip-attached to
664 a bead, and within the threshold tip separation at t seconds, and d_{tot} is the total number of microtubule
665 pairs that exceeded the threshold tip separation between time $t-1$ and t seconds for both survival
666 curves being compared. Expected values for each pair of survival curves were used to calculate a chi-
667 square value for each tip separation threshold using the following equation:

$$\chi^2 = \sum_{j=1}^{2} \frac{\left(\sum_{t=1}^{T} S_j(t) - \sum_{t=1}^{T} E_j(t)\right)^2}{\sum_{t=1}^{T} E_j(t)}$$

668 where T is the total number of timepoints (400, in all cases), $S_j(t)$ is the Kaplan-Meier survival
669 probability of curve j at time t, and $E_j(t)$ is the expected value of Kaplan-Meier survival curve j at time
670 t. A chi-square table was then used to estimate the p-value for each tip separation threshold.

671 To determine whether tip separation and tip separation speed between soft and stiff couplers
672 were statistically significant, we calculated p-values with a Wilcoxon-Mann-Whitney two sample rank
673 test using built-in Igor Pro software (Cheung & Klotz, 1997; Klotz, 2006; Streitberg & Rohmel, 1986; Zar,
674 1999).
675

676 **Figures**

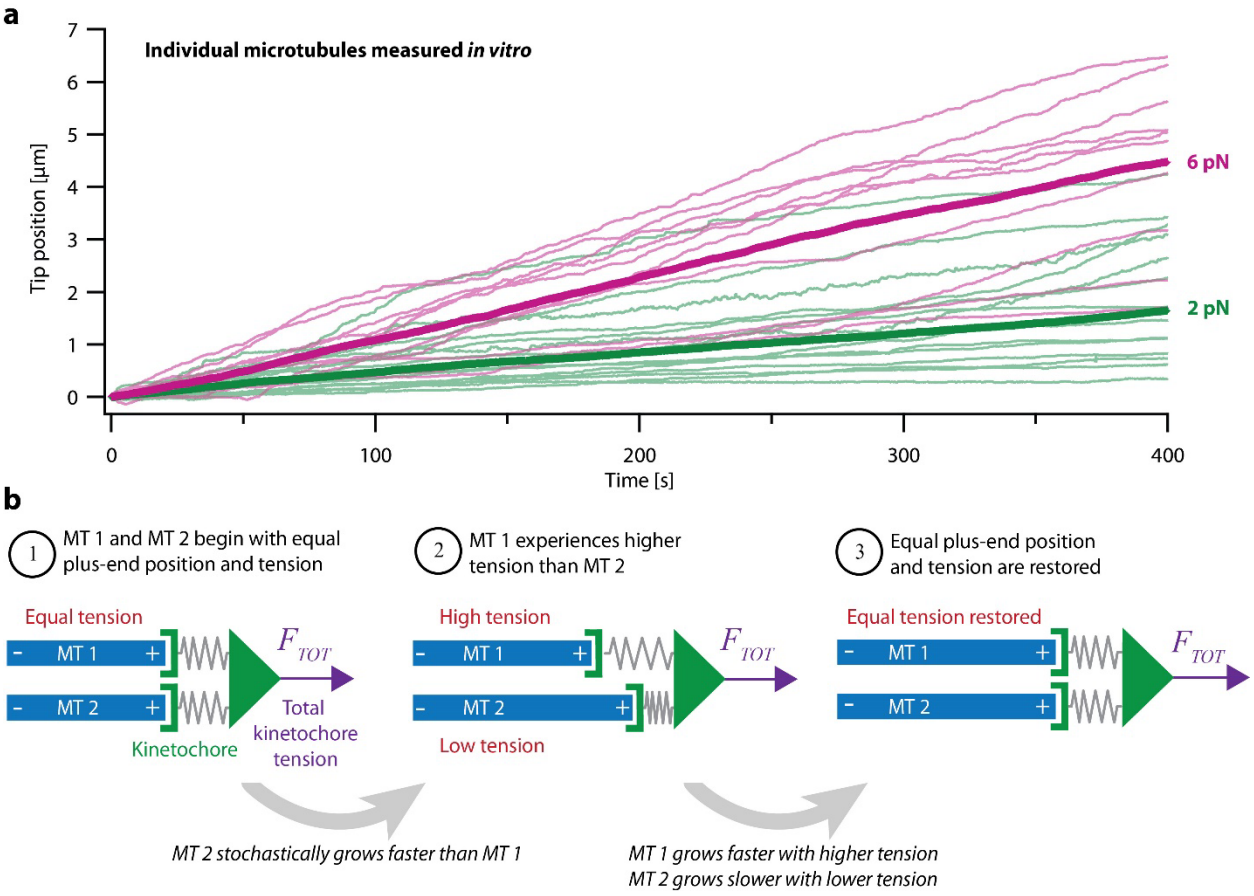

677
678

679 **Figure 1. Intrinsic variability in microtubule growth could be coordinated by mechanical coupling.** (**a**) Microtubules (MTs)
680 grow at intrinsically variable rates that increase with force, on average. Example recordings show plus-end position versus time
681 for individual growing microtubules subject to a constant tensile force of either 2 or 6 pN (thin green or magenta traces,
682 respectively). At each force, 10 to 14 example recordings are shown, together with the mean position versus time (thick traces,
683 computed from N = 25 or N = 10 individual recordings at 2 or 6 pN, respectively). Individual traces are from (Akiyoshi et al.,
684 2010). (**b**) Mechanism by which mechanical coupling could coordinate growing microtubules. In this example, two microtubules
685 share a total force, F_{TOT}, through two spring-like connections to their plus-ends. If one microtubule stochastically lags behind, it
686 will experience more tension than the leading microtubule due to differential stretching of their spring-connections. Because
687 tension tends to accelerate plus-end growth (as illustrated in panel a), the higher tension will tend to accelerate the growth of
688 the lagging microtubule, causing it to catch up.

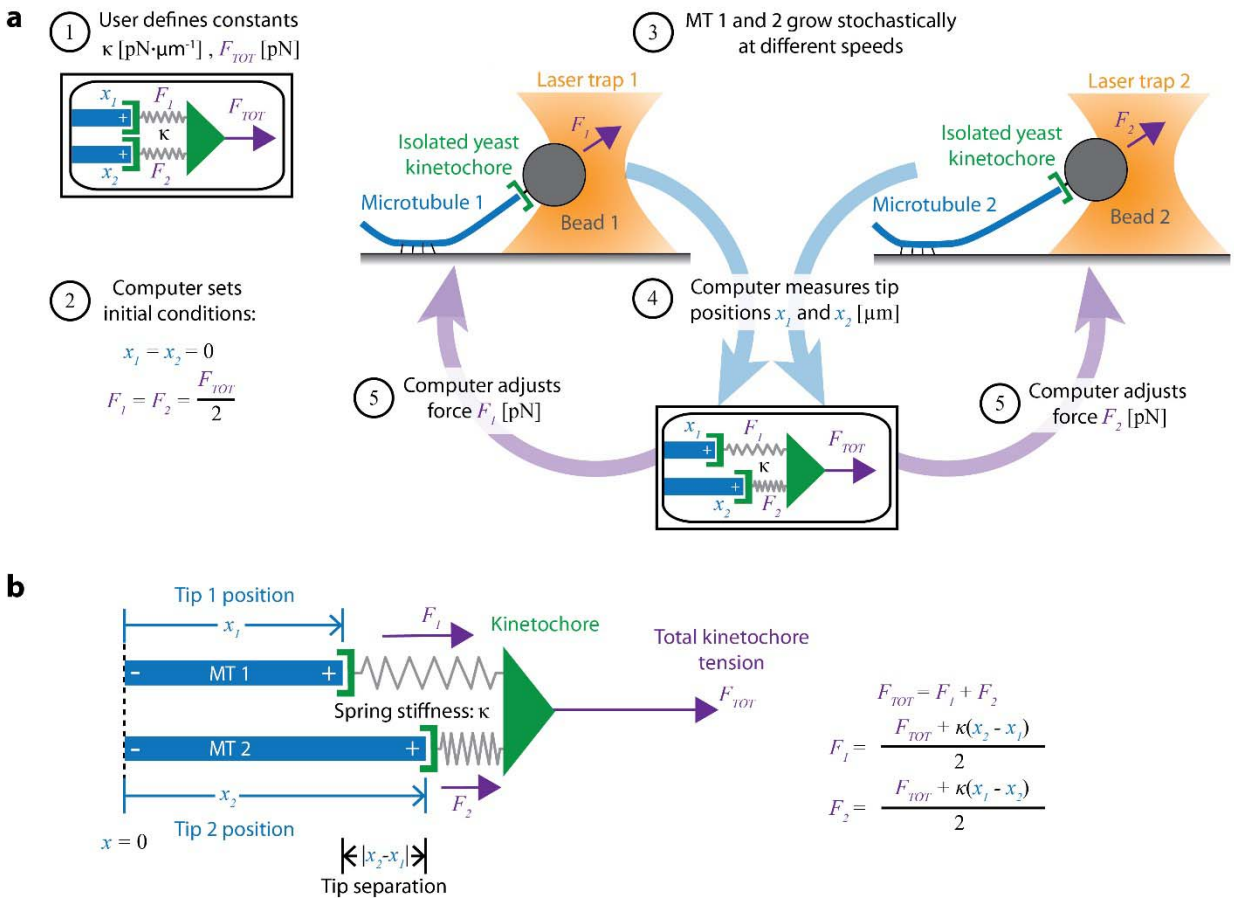

Figure 2. Dual-trap assay to measure the coordination of two real microtubules *in vitro* coupled together by simulated spring-like connections to a shared tensile load. (**a**) Schematic of the dual-trap assay, which measures the effects of the spring-coupler model (detailed in b) on real microtubules (MTs) growing *in vitro*. Two dynamic microtubules are grown from seeds anchored to two separate coverslips on two separate stages, each with their own microscope and laser trap. Each laser trap applies tension to its respective microtubule plus-end via a bead decorated with isolated yeast kinetochores, and each tension is adjusted dynamically under feedback control by a shared computer. Initially (steps 1 and 2), microtubule plus-ends are considered to have the same position ($x_1 = x_2 = 0$) so that each bears half of the total user-input tension (F_{TOT}). Over time, as microtubules grow at different rates (step 3), the computer dynamically adjusts the tension on each microtubule according to the spring-coupler model (steps 4 and 5), so that the higher the tip separation ($|x_1 - x_2|$) and stiffness (κ), the larger the difference in tension between the two microtubules. (**b**) Spring-coupler model used to represent the physical connection between two microtubule plus-ends via a kinetochore. Both springs have identical stiffnesses (κ). The kinetochore is assumed to be in force equilibrium such that the sum of the spring forces is equal to the total external force, F_{TOT}, which is kept constant in the current study.

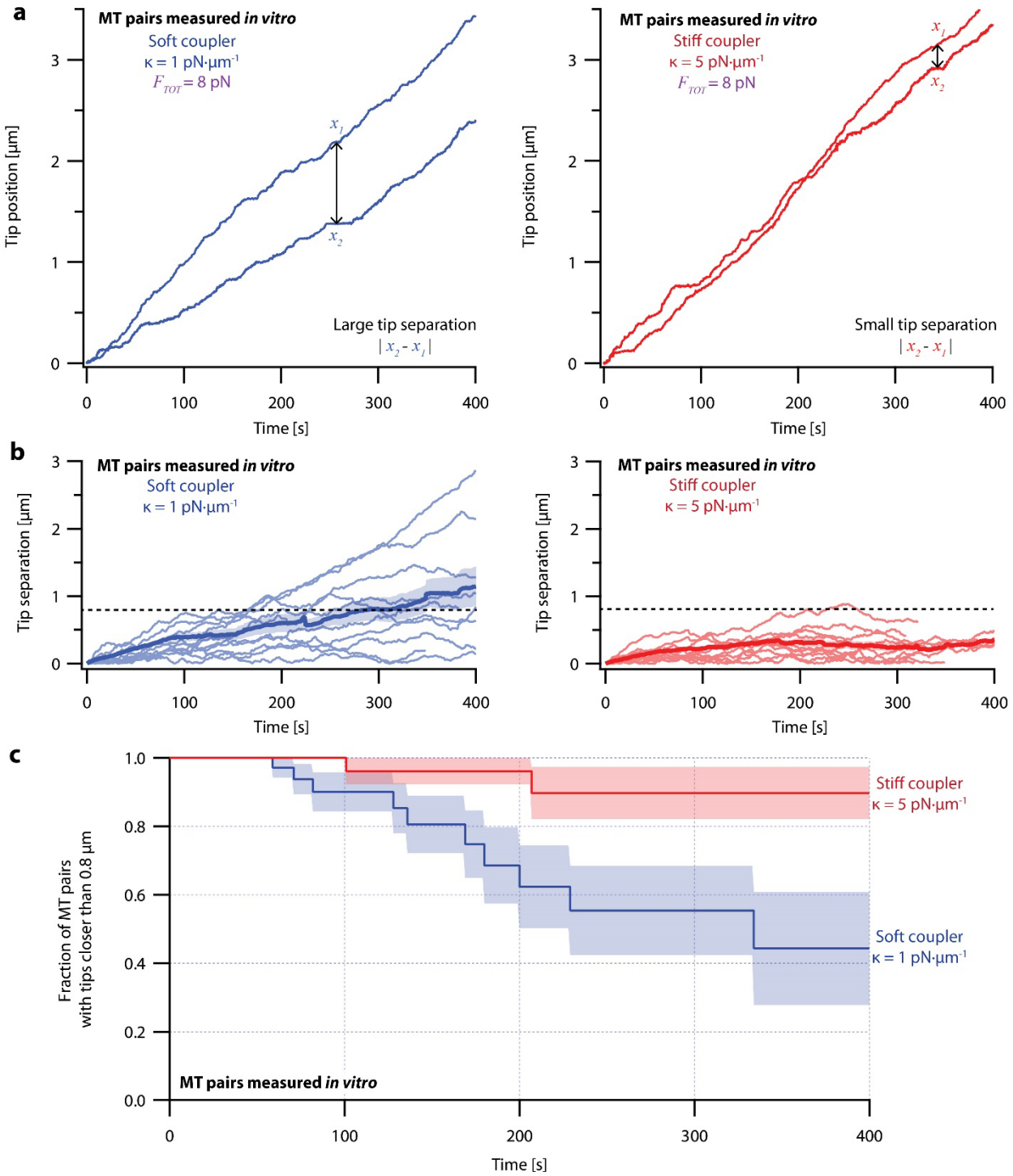

Figure 3. Microtubule pairs growing *in vitro* are coordinated by mechanical coupling. (**a**) Example dual-trap assay recordings showing real microtubule (MT) plus-end positions over time for representative microtubule pairs coupled via soft (1 pN·µm^{-1}, left) or stiff (5 pN·µm^{-1}, right) simulated spring-couplers. All dual-trap data was recorded with F_{TOT} = 8 pN. (**b**) Tip separation ($|x_1 - x_2|$) between microtubule plus-end pairs that were coupled with either soft (left) or stiff (right) simulated spring-couplers over 400 s of growth. Light colors show tip separations for 10 individual microtubule pairs with each coupler stiffness, while dark colors show mean tip separation for all recorded pairs (N = 50 and N = 43 recordings with soft and stiff couplers, respectively). (**c**) Fraction of microtubule pairs whose plus-ends remained within 0.8 µm of each other over time. (In other words, the fraction of pairs at any given time whose tip separation had not exceeded the dashed line in (b).) Shaded regions in (b) and (c) show SEMs from N = 50 and N = 43 recordings with soft and stiff couplers, respectively.

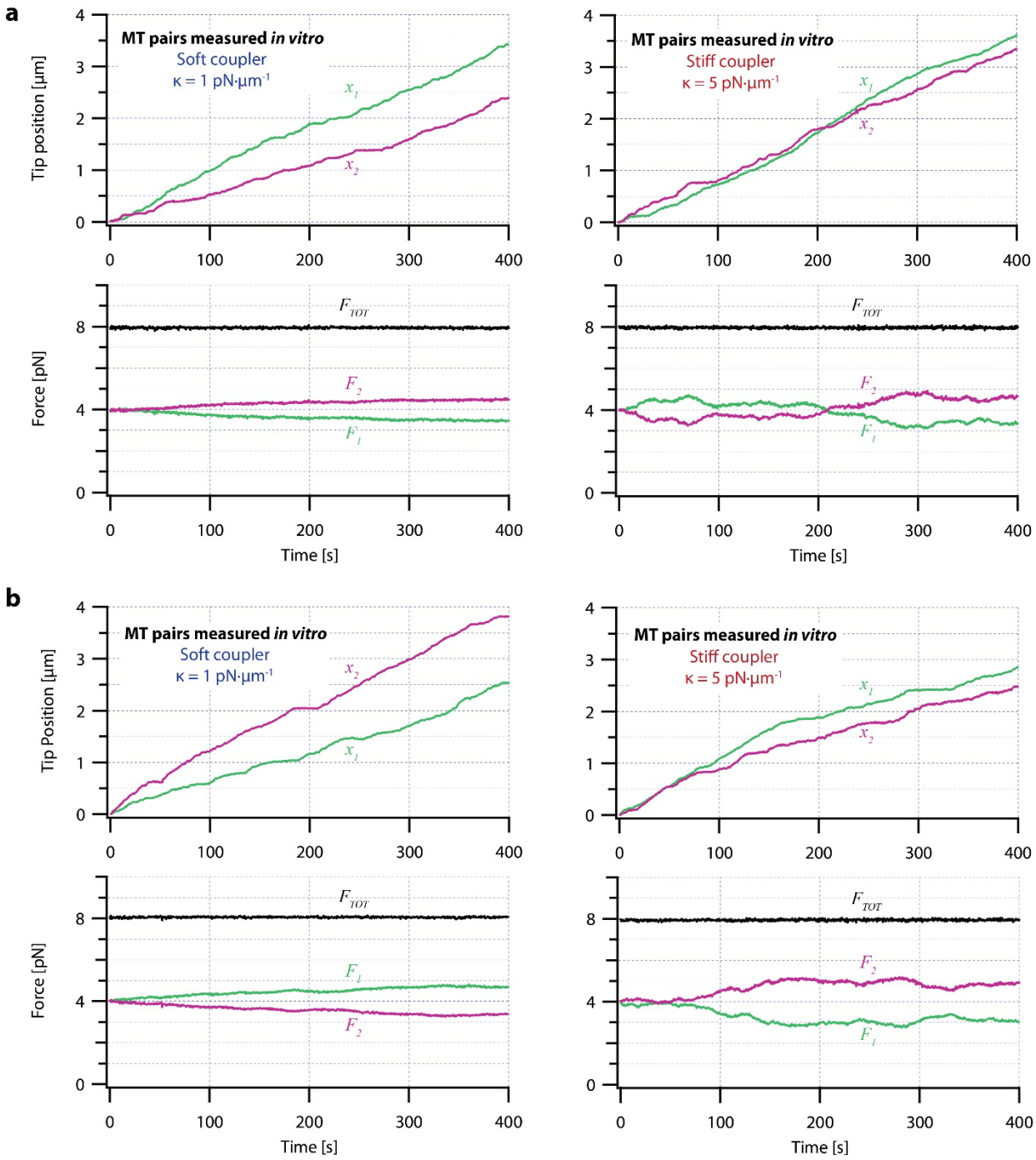

Figure S3-1. Additional dual-trap assay recordings showing tip positions and forces on pairs of growing microtubules. (**a**) Example dual-trap assay recordings showing real microtubule (MT) plus-end positions (top) and forces (bottom) plotted against time for representative microtubule pairs coupled via soft or stiff simulated spring-couplers. Plus-end position data in the top graphs is recopied from Figure 3a. Black traces in the bottom graphs show total force on the two microtubules (F_{TOT}) and demonstrate that a constant total force of F_{TOT} = 8 pN was maintained by the feedback-control. (**b**) Two additional examples of dual-trap assay recordings, formatted as in (a).

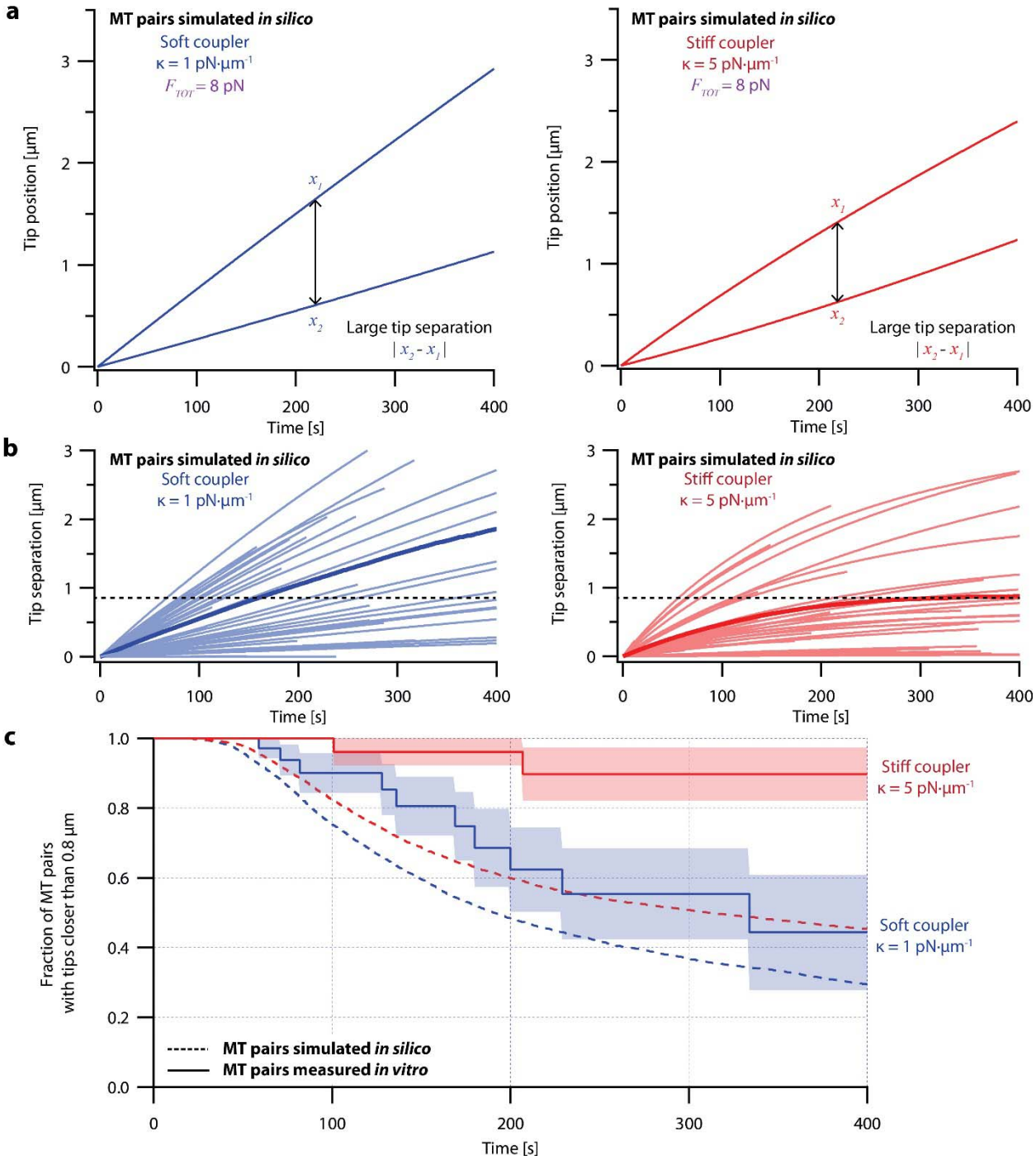

Figure 4. Simple non-pausing simulations fail to recapitulate the coordinated growth of mechanically coupled microtubule pairs. (**a**) Example simulations of microtubule (MT) plus-end positions over time using the non-pausing model. Simulated microtubule pairs were coupled via soft or stiff spring-couplers and shared a total load F_{TOT} = 8 pN to match dual-trap assay conditions. (**b**) Tip separations between microtubule plus-end pairs that were simulated using the non-pausing model and coupled with either soft (left) or stiff (right) spring-couplers. Light colors show tip separations for N = 40 individual simulated microtubule pairs, while dark colors show mean tip separation for N = 10,000 simulated pairs. (**c**) Comparison between the fraction of *in silico* (simulated, dashed curves) and *in vitro* (real, solid curves) microtubule pairs whose plus-ends remained within 0.8 μm of each other over time. Shaded regions show SEMs from N = 50 and N = 43 *in vitro* recordings with soft and stiff couplers, respectively. Soft- and stiff-coupled microtubule pairs were each simulated N = 10,000 times over 400 s of growth in both (b) and (c). Simulation parameters for (a), (b), and (c) can be found in Table 1.

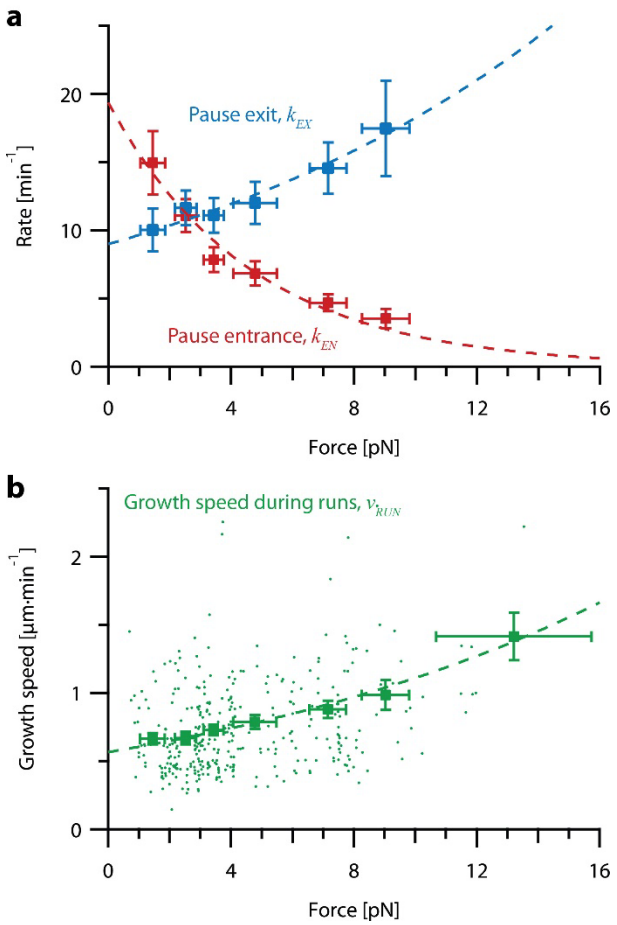

Figure 5. Increasing tension on individual growing microtubules suppresses pausing and accelerates growth during runs. (**a**) As tension on a growing microtubule tip increases, the rate of pause entrance decreases, while the rate of pause exit increases. Mean pause entrance (■) and exit (■) rates (k_{EN} and k_{EX}) were estimated as described in Figure S5-1 and are plotted as functions of force. Error bars show counting uncertainties from N = 25 to 85 individual microtubule recordings and dashed curves show least squares exponential fits. (**b**) As tension on a microtubule tip increases, the growth during runs (i.e., in-between pauses) is accelerated. Points show run speeds measured from recordings of individual microtubules subject to constant tensile forces (from (Akiyoshi et al., 2010)). Symbols (■) represent mean run speeds (v_{RUN}) grouped according to the applied tensile force. Error bars show SEMs from N = 9 to 85 individual microtubule recordings and dashed curve shows the least squares exponential fit. See Figure S5-1 and Materials and Methods for details and Table 1 for fit parameters.

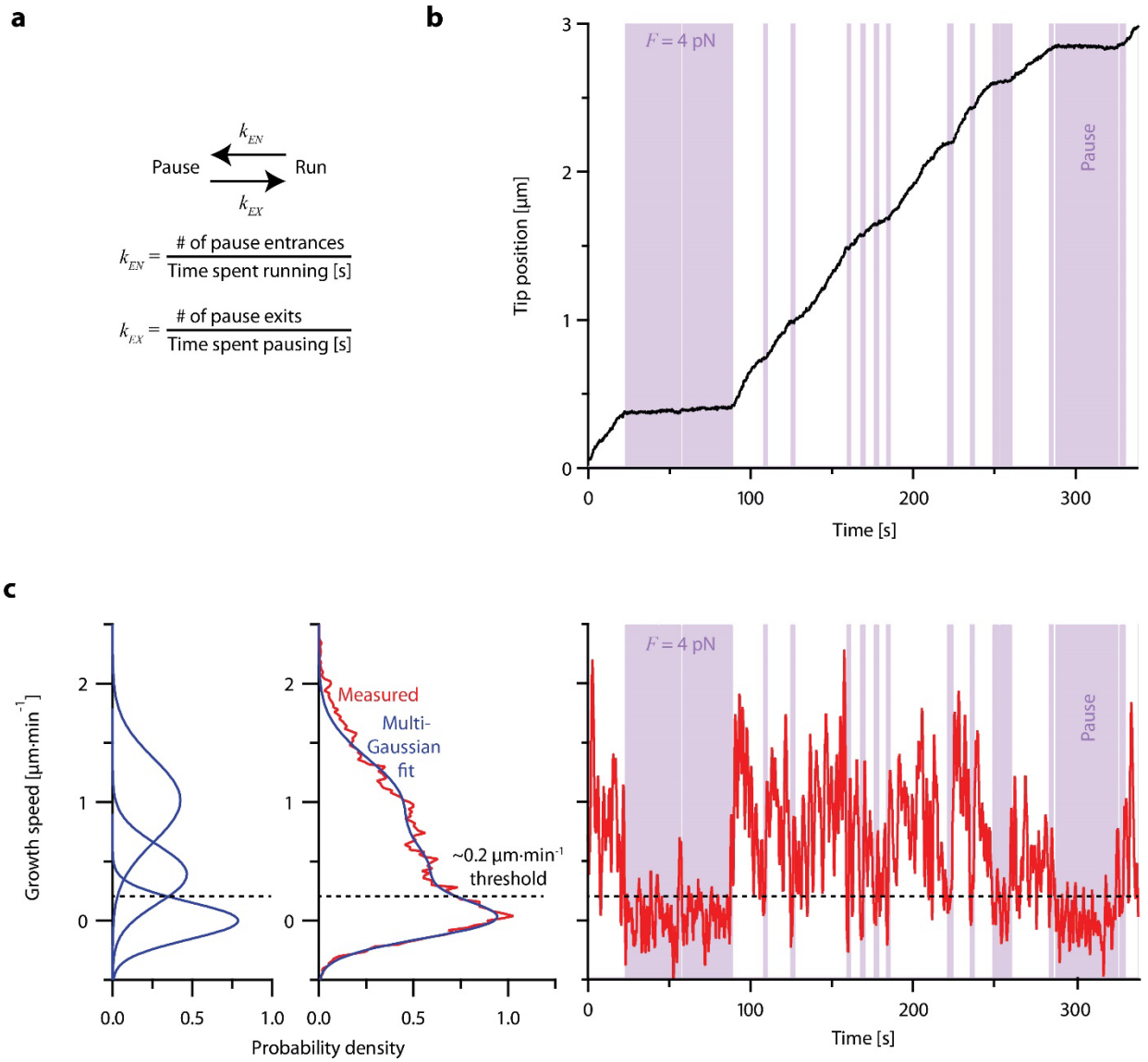

Figure S5-1. Individual microtubules frequently pause during periods of overall growth. (**a**) Growing microtubules switch between states of 'pause,' when plus-end growth speed is nearly zero, and 'run,' when the plus-end is clearly growing. Pause entrance and exit rates, k_{EN} and k_{EX}, were quantified by counting the numbers of entrances or exits and dividing by the total amount of time spent in the run or pause states, respectively. (**b**) Example recording showing plus-end position versus time for an individual microtubule subject to a constant tensile force of 4 pN and exhibiting frequent pauses (denoted by purple shaded regions). This example recording is one of N = 356 force-clamp traces (from (Akiyoshi et al., 2010)) used to estimate the pause entrance and exit rates and growth speeds during runs as functions of force (as shown in Figure 5). (**c**) Classification of runs and pauses. Instantaneous growth speed was computed as a function of time (and plotted at right) from the recording shown in (b), using a 2 s sliding window, and then assembled into a histogram (middle plot, red) and fit with a sum of multiple Gaussian curves (middle and left plots, blue). One Gaussian was always centered at 0 µm·min^{-1} and defined as the 'pause' peak. The intersection of the pause peak and the Gaussian having the next highest mean growth speed was identified for each individual recording and used as a threshold (dashed horizontal line) to distinguish pauses and runs for that recording. Pauses were defined as periods longer than 1 s when the instantaneous growth speed fell below the threshold, while runs were defined as periods longer than 1 s when growth speed was above the threshold (see Materials and Methods for details).

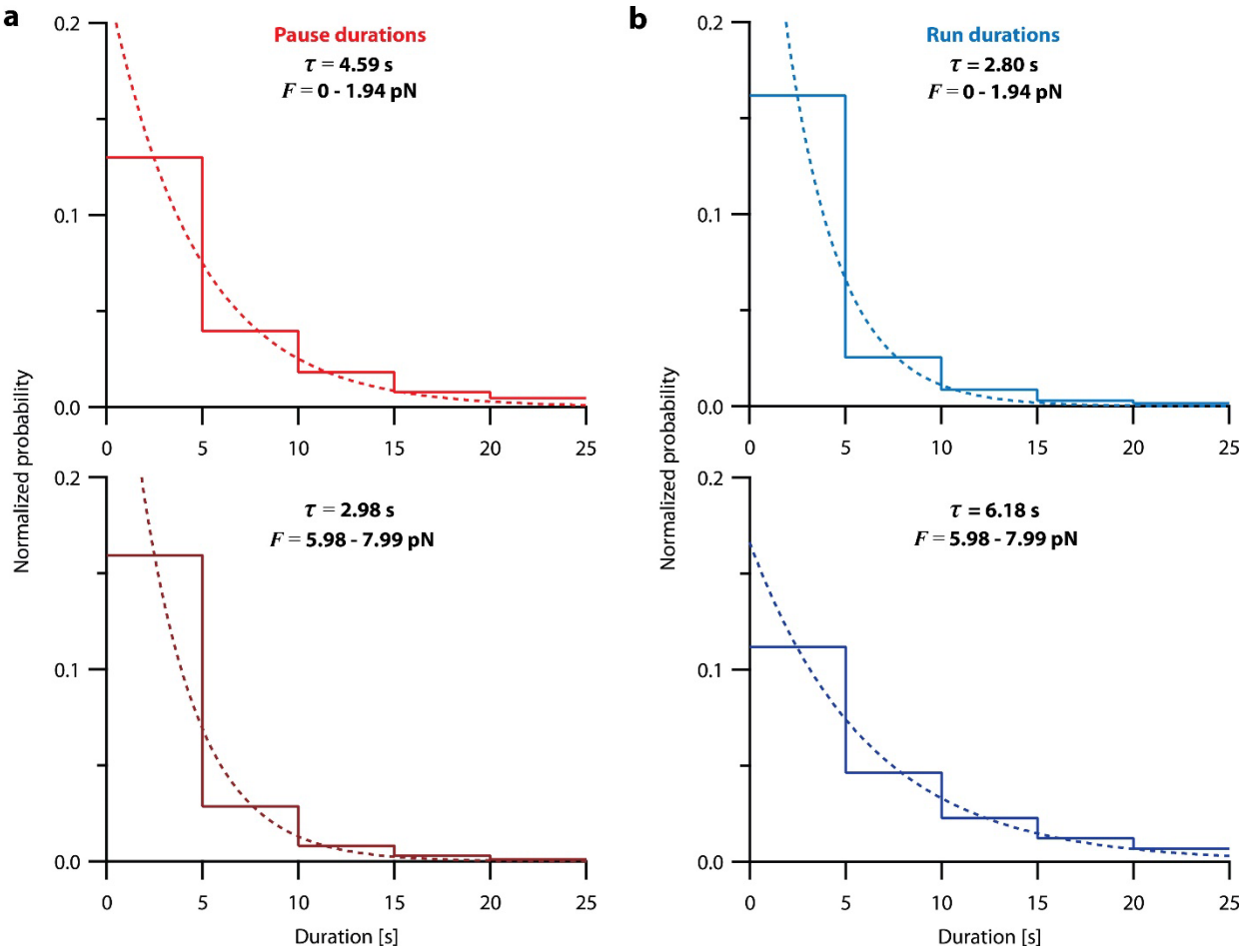

Figure S5-2. Pause and run durations are exponentially distributed. (**a**) Normalized histograms showing pause durations measured from recordings of individual microtubules growing under constant levels of tension (force-clamp data from (Akiyoshi et al., 2010)), either between 0 and 2 pN (top), or between 6 and 8 pN (bottom), corresponding to the lowest and third-highest force bins in Table 2, respectively. (**b**) Normalized histograms showing run durations measured from recordings of individual microtubules growing under constant levels of tension (force-clamp data from (Akiyoshi et al., 2010)), as in (a). For both (a) and (b), least-squares regressions are shown as dashed curves. The indicated time constants (τ) were derived from these fits.

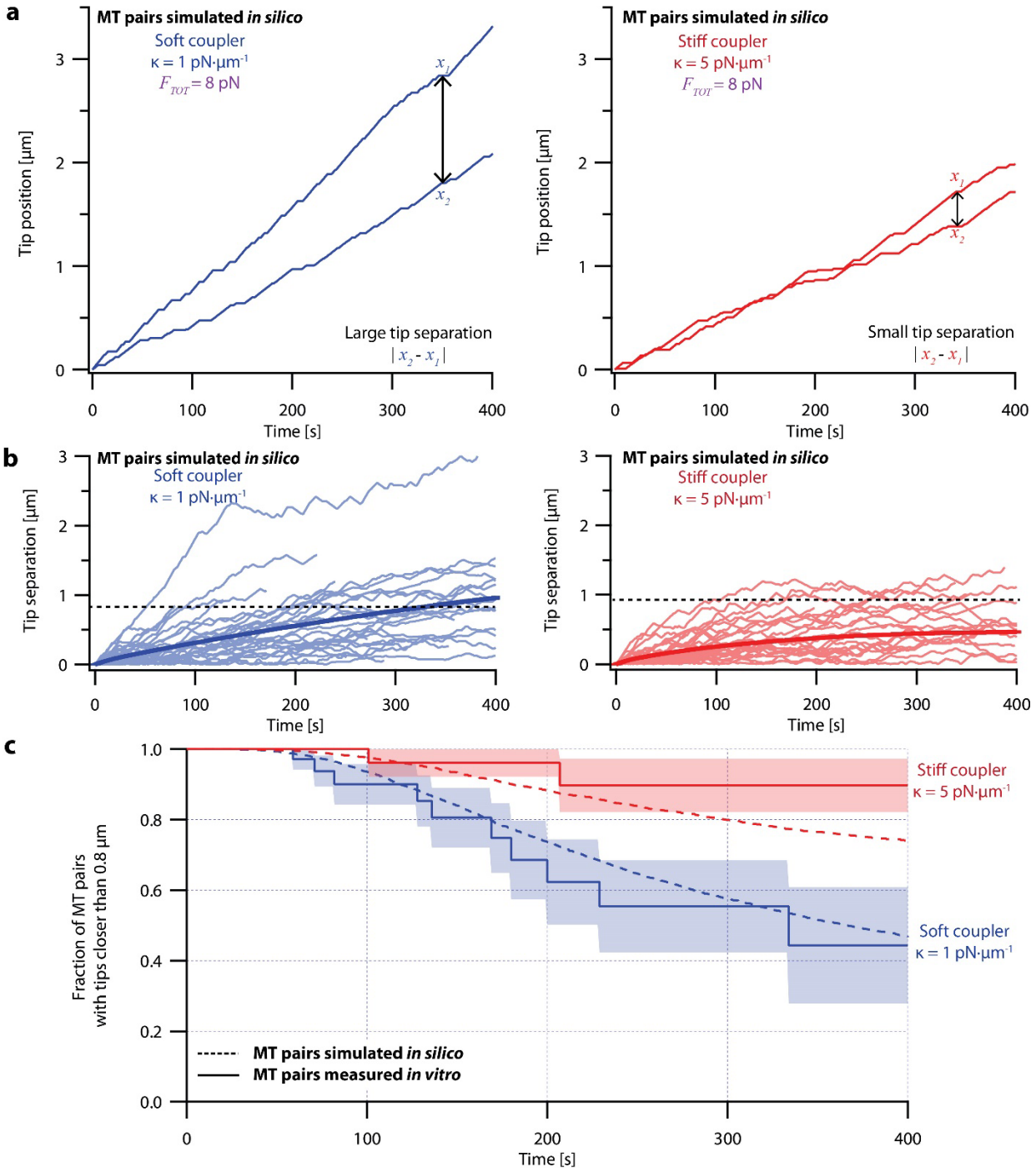

Figure 6. Simulations recapitulate the coordinated growth of mechanically coupled microtubule pairs. (**a**) Example simulations of microtubule (MT) plus-end positions over time using the pausing model. Simulated microtubule pairs were coupled via soft or stiff spring-couplers and shared a total load F_{TOT} = 8 pN to match dual-trap assay conditions. (**b**) Tip separations between microtubule plus-end pairs that were simulated using the pausing model and coupled with either soft (left) or stiff (right) spring-couplers. Light colors show tip separations for N = 40 individual simulated microtubule pairs, while dark curves show mean tip separation for N = 10,000 simulated pairs. (**c**) Comparison between the fraction of *in silico* (simulated, dashed curves) and *in vitro* (real, solid curves) microtubule pairs whose plus-ends remained within 0.8 μm of each other over time. Shaded regions show SEMs from N = 50 and N = 43 *in vitro* recordings with soft and stiff couplers, respectively. Soft- and stiff-coupled microtubule pairs were each simulated N = 10,000 times over 400 s of growth in both (b) and (c). Simulation parameters for (a), (b), and (c) are listed in Table 1.

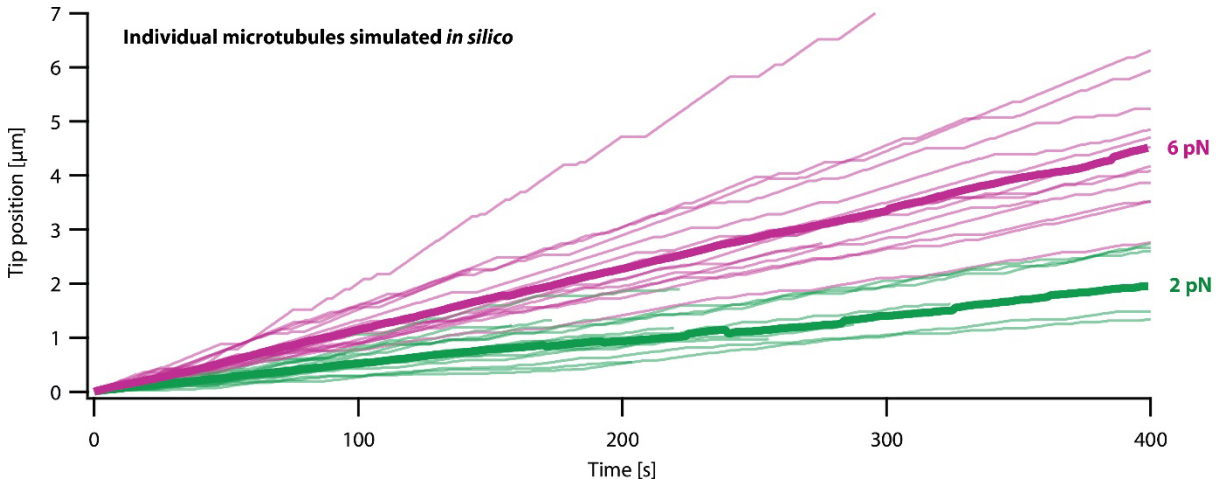

Figure S6-1. Simulations of microtubule growth under constant force using the pausing model resemble real microtubule recordings. Examples using the pausing model to simulate plus-end position versus time for individual growing microtubules subject to a constant tensile force of either 2 or 6 pN (light green or magenta traces, respectively). At each force, N = 16 example simulations are shown, together with the corresponding mean positions versus time (thick traces, computed from the N = 16 individual simulations).

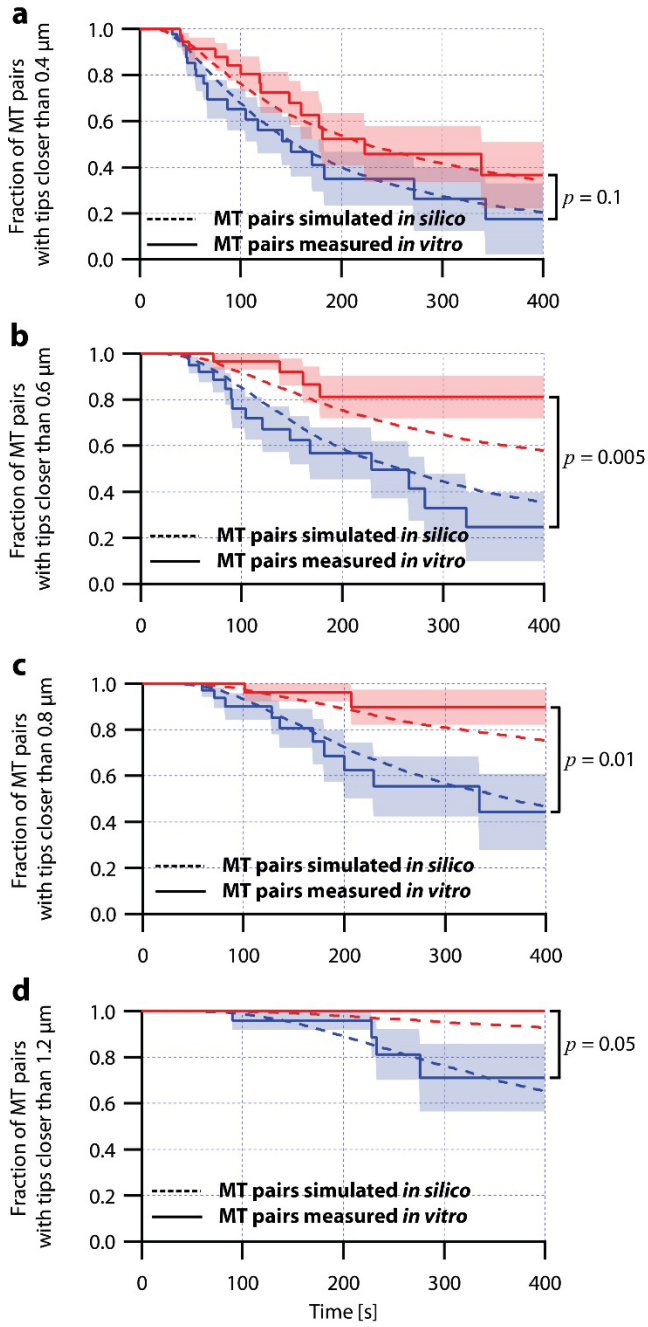

Figure S6-2. Simulations of microtubule pairs using the pausing model maintain tip separations similar to real microtubule pairs. Comparison between the fraction of *in silico* (simulated, dashed curves) and *in vitro* (real, solid curves) microtubule (MT) pairs whose plus-ends remained within (**a**) 0.4 µm, (**b**) 0.6 µm, (**c**) 0.8 µm, and (**d**) 1.2 µm of each other over time. Microtubule pairs *in silico* and *in vitro* shared a total load of F_{TOT} = 8 pN and were coupled via soft or stiff spring couplers. Shaded regions show SEM from N = 50 and N = 43 *in vitro* recordings with soft and stiff couplers, respectively. Soft- and stiff-coupled microtubule pairs were each simulated N = 10,000 times over 400 s of growth. Simulation parameters can be found in Table 1. P-values indicate comparisons between soft- and stiff-coupled microtubule pairs *in vitro* using a log-rank test.

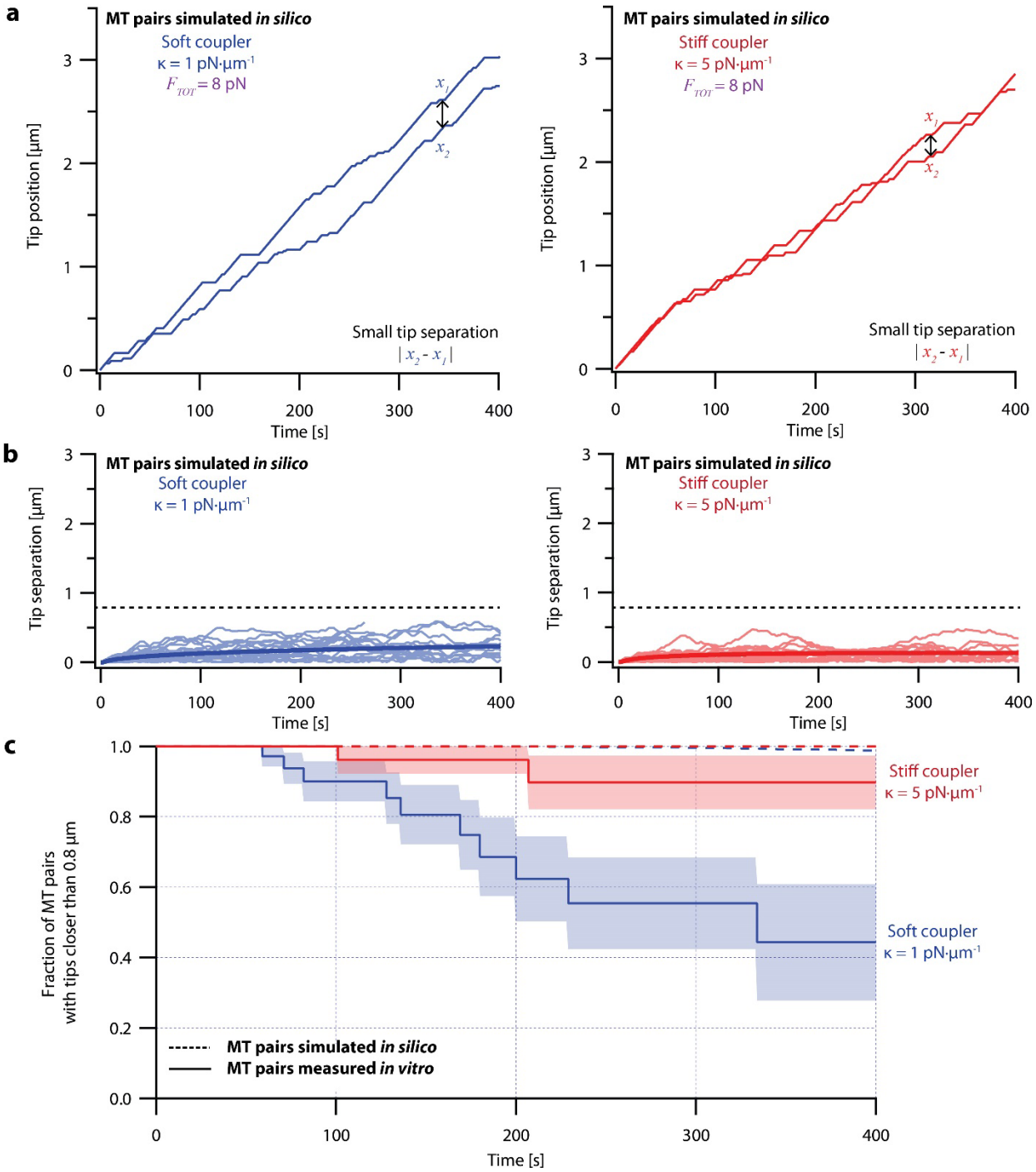

Figure S6-3. Simulations using an ergodic version of the pausing model, without intrinsic heterogeneity, fail to recapitulate the coordinated growth of mechanically coupled microtubules pairs. (**a**) Example simulations of microtubule (MT) plus-end positions over time using the ergodic pausing model. Simulated microtubule pairs were coupled via soft or stiff spring-couplers and shared a total load F_{TOT} = 8 pN to match dual-trap assay conditions. (**b**) Tip separations between microtubule plus-end pairs that were simulated using the ergodic pausing model and coupled with either soft (left) or stiff (right) spring-couplers. Light colors show tip separations for N = 40 individual simulated microtubule pairs while dark colors show mean tip separation for N = 10,000 simulated pairs. (**c**) Comparison between the fraction of *in silico* (simulated, dashed curves) and *in vitro* (real, solid curves) microtubule pairs whose plus-ends remained within 0.8 μm of each other over time. Shaded regions show SEMs from N = 50 and N = 43 *in vitro* recordings with soft and stiff couplers, respectively. Soft- and stiff-coupled microtubule pairs

were each simulated N = 10,000 times over 400 s of growth in both (b) and (c). Simulation parameters for (a), (b), and (c) can be found in Table 1. As expected, microtubule pairs simulated using this ergodic model remained much closer together than real microtubule pairs, rarely separating by more than 0.5 µm irrespective of coupler stiffness. After 300 s, the average tip separation for soft-coupled pairs was only 0.202 ± 0.002 µm (mean ± SEM from N = 10,000 simulations), barely different from the average tip separation for stiff-coupled pairs of 0.134 ± 0.002 µm (mean ± SEM from N = 10,000 simulations). Combined with the success of the non-ergodic pausing model in fitting our dual-trap data, this supports the idea that microtubule growth can be considered non-ergodic during our 400 s experiments.

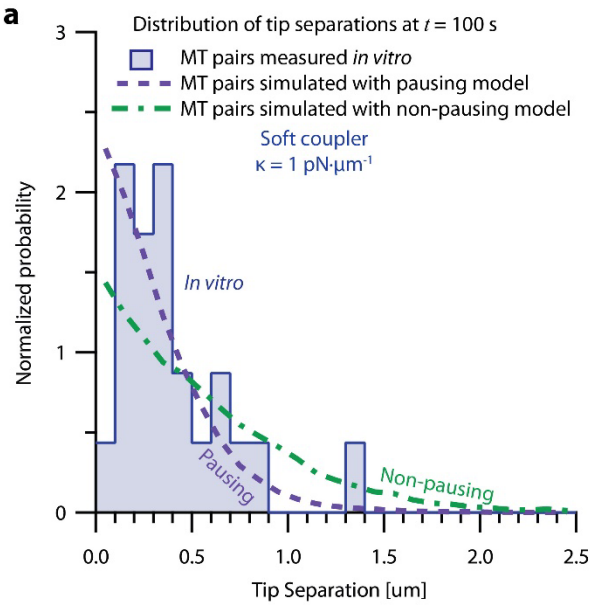

	Mean [μm]	SD [μm]	SEM [μm]	N	Log Likelihood
In vitro	0.39	0.29	0.06	23	N/A
Pausing	0.32	0.27	0.0009	100,397	-15.6
Non-pausing	0.56	0.49	0.002	100,654	-16.3

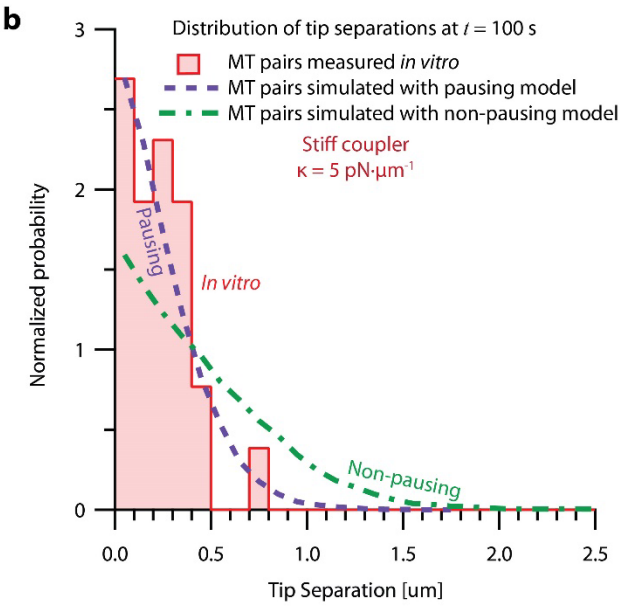

	Mean [μm]	SD [μm]	SEM [μm]	N	Log Likelihood
In vitro	0.23	0.17	0.03	26	N/A
Pausing	0.25	0.21	0.0007	100,000	-10.2
Non-pausing	0.45	0.37	0.001	100,000	-13.4

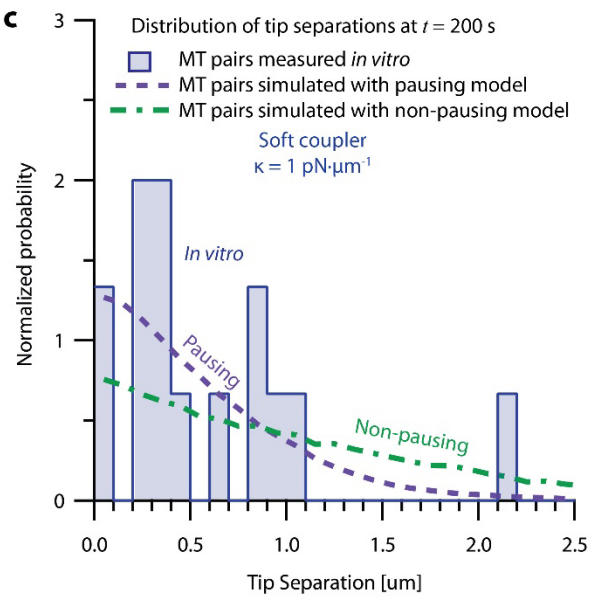

	Mean [μm]	SD [μm]	SEM [μm]	N	Log Likelihood
In vitro	0.60	0.54	0.17	15	N/A
Pausing	0.56	0.48	0.0015	100,000	-18.0
Non-pausing	1.05	0.91	0.0028	104,792	-19.2

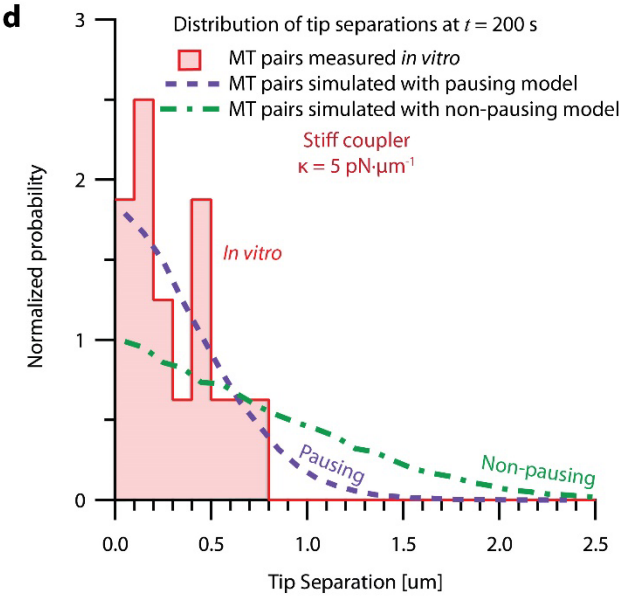

	Mean [μm]	SD [μm]	SEM [μm]	N	Log Likelihood
In vitro	0.31	0.23	0.06	16	N/A
Pausing	0.37	0.29	0.00092	100,000	-14.5
Non-pausing	0.71	0.55	0.0017	100,000	-17.3

Figure S6-4. Probability analysis shows pausing model fits dual-trap recordings better than the non-pausing model. (**Top of each panel**) Histograms of tip separation between microtubule pairs measured in the dual-trap assay and simulated using the pausing and non-pausing model. Soft-coupled pairs are shown on the left ((**a**) and (**c**)), while stiff-coupled pairs are shown on the right ((**b**) and (**d**)). Histograms of tip separations measured 100 s after the start of the recording or simulation are shown on the top ((**a**) and (**b**)), while tip separations measured 200 s after the start of the recording or simulation are shown on the bottom ((**c**) and (**d**)). Tip separation histograms produced by the pausing (purple) and non-pausing model (green) are represented with dashed lines, while dual-trap data is represented by bars. (**Bottom of each panel**) Tables comparing the means, standard deviations (SD), standard errors of the mean (SEM) and numbers of recordings (N) for *in vitro* microtubule pairs and microtubule pairs simulated using the pausing and non-pausing models. The log likelihood probability for each model given the *in vitro* data is shown in the righthand column. The greater the log likelihood, the greater the probability that the given model could reproduce the measured *in vitro* data. At both 100 s and 200s, for soft and stiff couplers, the pausing model scores higher than the non-pausing model, indicating that the pausing model is a better fit to our *in vitro* data.

Parameter name	Parameter symbol	Relevant equation	Parameter estimate	Applicable models	Reference
Growth speed force sensitivity	F_g	$v_g = v_{g0}\exp(F/F_g)$	8.4 pN	non-pausing	Akiyoshi et al., 2010 Figure 4e
Unloaded pause entrance rate	k_{EN0}	$k_{EN} = k_{EN0}\exp(F/F_{EN})$	19.4 min^{-1}	pausing	Figure 5a, red
Pause entrance rate force sensitivity	F_{EN}	$k_{EN} = k_{EN0}\exp(F/F_{EN})$	-4.6 pN	pausing	Figure 5a, red
Unloaded pause exit rate	k_{EX0}	$k_{EX} = k_{EX0}\exp(F/F_{EX})$	9.0 min^{-1}	pausing	Figure 5a, blue
Pause exit rate force sensitivity	F_{EX}	$k_{EX} = k_{EX0}\exp(F/F_{EX})$	14.1 pN	pausing	Figure 5a, blue
Unloaded run speed	v_0	$v_{RUN} = v_0\exp(F/F_{RUN})$	0.52 $\mu m \cdot min^{-1}$	neither	Figure 5b
Run speed force sensitivity	F_{RUN}	$v_{RUN} = v_0\exp(F/F_{RUN})$	14.8 pN	pausing	Figure 5b

Table 1. Parameter table for coupled microtubule pairs simulated for non-pausing and pausing models. Relevant parameters measured from constant force recordings from (Akiyoshi et al., 2010). These parameters were used to simulate coupled microtubule pairs using each of the models described in the main text. The equation in which each parameter is used, as well as which models of microtubule growth use that equation, are indicated.

Bin number	N	Lower bound [pN]	Upper bound [pN]	Pause entrances	Time in pause [s]	Pause exits	Time in run [s]
1	41	0.69	1.94	1834	10957	1830	7364
2	85	1.94	2.97	3502	18047	3501	18952
3	77	2.97	3.999	2376	12842	2374	18159
4	60	3.999	5.98	1937	9661	1932	16993
5	60	5.98	7.99	1439	5930	1438	18465
6	25	7.99	10.3	387	1298	378	6559
7	9	10.3	18	23	93	23	712

Table 2. Number of recordings, bounds, and pause quantification from force-clamp dataset, binned by force. Table describing constant force recordings in (Akiyoshi et al., 2010) and the pause quantification performed in the current work. N indicates the number of recordings in a particular bin. For consistency, these force bins are identical to those used in (Akiyoshi et al., 2010).

References

Akiyoshi, B., Sarangapani, K. K., Powers, A. F., Nelson, C. R., Reichow, S. L., Arellano-Santoyo, H., Gonen, T., Ranish, J. A., Asbury, C. L., & Biggins, S. (2010). Tension directly stabilizes reconstituted kinetochore-microtubule attachments. *Nature*, *468*(7323), 576-579. https://doi.org/10.1038/nature09594

Al-Bassam, J., Kim, H., Brouhard, G., van Oijen, A., Harrison, S. C., & Chang, F. (2010). CLASP promotes microtubule rescue by recruiting tubulin dimers to the microtubule. *Dev Cell*, *19*(2), 245-258. https://doi.org/10.1016/j.devcel.2010.07.016

Amaro, A. C., Samora, C. P., Holtackers, R., Wang, E., Kingston, I. J., Alonso, M., Lampson, M., McAinsh, A. D., & Meraldi, P. (2010). Molecular control of kinetochore-microtubule dynamics and chromosome oscillations. *Nature Cell Bio*, *12*(4), 319-329. https://doi.org/10.1038/ncb2033

Amin, M. A., Agarwal, S., & Varma, D. (2019). Mapping the kinetochore MAP functions required for stabilizing microtubule attachments to chromosomes during metaphase. *Cytoskeleton*, *76*(6), 398-412. https://doi.org/10.1002%2Fcm.21559

Amoah-Darko, F. L., & White, D. (2022). Modelling microtubule dynamic instability: Microtubule growth, shortening and pause. *J Theor Biol*, *553*, 111257-111257. https://doi.org/10.1016/j.jtbi.2022.111257

Asbury, C. L., Gestaut, D. R., Powers, A. F., Franck, A. D., & Davis, T. N. (2006). The Dam1 kinetochore complex harnesses microtubule dynamics to produce force and movement. *Proc Natl Acad Sci U S A*, *103*(26), 9873-9878. https://doi.org/10.1073/pnas.0602249103

Bakhoum, S. F., & Compton, D. A. (2012). Kinetochores and disease: keeping microtubule dynamics *in check! Curr Opinion in Cell Biol*, *24*(1), 64-70. https://doi.org/10.1016/j.ceb.2011.11.012

Bakhoum, S. F., Genovese, G., & Compton, D. A. (2009). Deviant kinetochore microtubule dynamics underlie chromosome instability. *Curr Biol*, *19*(22), 1937-1942. https://doi.org/10.1016/j.cub.2009.09.055

Banigan, E., Chiou, K., Ballister, E. R., Mayo, A. M., Lampson, M. A., & Liu, A. J. (2015). Minimal model for collective kinetochore-microtubule dynamics. *PNAS*, *112*(41), 12699-12704. https://doi.org/10.1073/pnas.1513512112

Brouhard, G., & Rice, L. M. (2018). Microtubule Dynamics: an interplay of biochemistry and mechanics. *Nat Rev Mol Cell Biol*, *19*(7), 451-463. https://doi.org/10.1038/s41580-018-0009-y

Brouhard, G. J. (2015). Dynamic instability 30 years later: complexities in microtubule growth and catastrophe. *MBoC*, *26*(7), 1207-1210. https://doi.org/10.1091/mbc.E13-10-0594

Brouhard, G. J., Stear, J. H., Noetzel, T. L., Al-Bassam, J., Kinoshita, K., Harrison, S. C., Howard, J., & Hyman, A. A. (2008). XMAP215 is a processive microtubule polymerase. *Cell*, *132*(1), 79-88. https://doi.org/10.1016/j.cell.2007.11.043

882 Cassimeris, L., Pryer, N. K., & Salmon, E. D. (1988). Real-time observations of microtubule dynamic
883 instability in living cells. *J Cell Biol*, *107*(6), 2223-2231. https://doi.org/10.1083/jcb.107.6.2223
884
885 Castrogiovanni, C., Inchingolo, A. V., Harrison, J. U., Dudka, D., Sen, O., Burroughs, N. J., McAinsh, A. D.,
886 & Meraldi, P. (2021). Evidence for a HURP/EB free mixed nucleotide zone in kinetochore-microtubules.
887 *Nature communications*, *13*(1). https://doi.org/10.1038/s41467-022-32421-x
888
889 Chacon, J. M., Mukherjee, S., Schuster, B. M., Clarke, D. J., & Gardner, M. K. (2014). Pericentromere
890 tension is self-regulated by spindle structure in metaphase. *J Cell Biol*, *205*(3), 313-324.
891 https://doi.org/10.1083/jcb.201312024
892
893 Cheung, Y. K., & Klotz, J. H. (1997). The Mann Whitney Wilcoxon distribution using linked lists. *Statistica*
894 *Sinica*, *7*, 805-813. https://www3.stat.sinica.edu.tw/statistica/oldpdf/a7n316.pdf
895
896 Chretien, D., Metoz, F., Verde, F., Karsenti, E., & Wade, R. H. (1992). Lattice defects in microtubules:
897 protofilament numbers vary within individual microtubules. *J Cell Biol*, *117*(5), 1031-1040.
898 https://doi.org/10.1083/jcb.117.5.1031
899
900 Cimini, D., Cameron, L. A., & Salmon, E. D. (2004). Anaphase spindle mechanics prevent mis-segregation
901 of merotelically oriented chromosomes. *Curr Biol*, *14*(23), 2149-2155.
902 https://doi.org/10.1016/j.cub.2004.11.029
903
904 Cleary, J. M., & Hancock, W. O. (2021). Molecular mechanisms underlying microtubule growth dynamics.
905 *Curr Biol*, *31*(10), R560-R573. https://doi.org/10.1016/j.cub.2021.02.035
906
907 Cleary, J. M., Kim, T., Cook, A. S. I., McCormick, L. A., Hancock, W. O., & Rice, L. M. (2022).
908 Measurements and simulations of microtubule growth imply stron longitudinal interactions and reveal a
909 role for GDP on the elongating end. *Elife*, *11*. https://doi.org/10.7554/eLife.75931
910
911 Cojoc, G., Roscioli, E., Zhang, L., Garcia-Ulloa, A., Shah, J. V., Berns, M. W., Pavin, N., Cimini, D., Tolic, I.
912 M., & Gregan, J. (2016). Laser microsurgery reveals conserved viscoelastic behavior of the kinetochore. *J*
913 *Cell Biol*, *212*(7), 767-776. https://doi.org/10.1083/jcb.201506011
914
915 Coombes, C. E., Yamamoto, A., Kenzie, M. R., Odde, D. J., & Gardner, M. K. (2013). Evolving tip structures
916 can explain age-dependent microtubule catastrophe. *Curr Biol*, *23*(14), 1342-1348.
917 https://doi.org/10.1016/j.cub.2013.05.059
918
919 Das, D., Das, D., & Padinhateeri, R. (2014). Force-induced dynamical properties of multiple cytoskeletal
920 filaments are distinct from that of single filaments. *PLoS one*, *9*(12).
921 https://doi.org/10.1371/journal.pone.0114014
922
923 Dogterom, M., & Yurke, B. (1997). Measurement of the force-velocity relation for growing microtubules.
924 *Science*, *278*(5339), 856-860. http://www.ncbi.nlm.nih.gov/pubmed/9346483
925
926 Driver, J. W., Geyer, E. A., Bailey, M. E., Rice, L. M., & Asbury, C. L. (2017). Direct measurement of
927 conformational strain energy in protofilaments curling outward from disassembling microtubule tips.
928 *Elife*, *6*. https://doi.org/10.7554/eLife.28433
929

Drpic, D., Almeida, A. C., Aguiar, P., Renda, F., Damas, J., Lewin, H. A., Larkin, D., Khodjakov, A., & Maiato, H. (2018). Chromosome segregation is biased by kinetochore size. Curr Biol, 28(9), 1344-1356. https://doi.org/10.1016/j.cub.2018.03.023

Ertych, N., Stolz, A., Stenzinger, A., Weichert, W., KaulfuB, S., Burfeind, P., Aigner, A., Wordeman, L., & Bastians, H. (2014). Increased microtubule assembly rates influence chromosomal instability in colorectal cancer cells. *Nature Cell Bio*, *16*(8), 779-791. https://doi.org/10.1038/ncb2994

Franck, A. D., Powers, A. F., Gestaut, D. R., Davis, T. N., & Asbury, C. L. (2010). Direct physical study of kinetochore-microtubule interactions by reconstitution and interrogation with an optical force clamp. *Methods*, *51*(2), 242-250. https://doi.org/10.1016/j.ymeth.2010.01.020

Gardner, M. K., & Odde, D. J. (2010). Stochastic simulation and graphic visualization of mitotic processes. *Methods*, *51*(2), 251-256. https://doi.org/10.1016/j.ymeth.2010.01.021

Gardner, M. K., Pearson, C. G., Sprague, B. L., Zarzar, T. R., Bloom, K., Salmon, E. D., & Odde, D. J. (2005). Tension-dependent regulation of microtubule dynamics at kinetochores can explain metaphase congression in yeast. *Mol Biol Cell*, *16*(8), 3764-3775. https://doi.org/10.1091/mbc.E05-04-0275

Garner, R. M., & Theriot, J. A. (2022). Leading edge maintenance in migrating cells is an emergent property of branched actin network growth. *Elife*, *11*. https://doi.org/10.7554/eLife.74389

Gaudenz, D., Matov, A., Wittman, T., Kumar, P., Thoma, C., Applegate, K., & Krek, W. (2010). Analysis of microtubule dynamic instability using a plus-end growth marker. *Nature methods*, *7*(9), 761-768. https://doi.org/10.1038/NMETH.1493

Geisterfer, Z. M., Zhu, D. Y., Mitchison, T. J., Oakey, J., & Gatlin, J. C. (2020). Microtubule growth rates are sensitive to global and local changes in microtubule plus-end density. *Curr Biol*, *30*(15), 3016-3023. https://doi.org/10.1016/j.cub.2020.05.056

Ghanti, D., & Chowdhury, D. (2015). Collective cargo hauling by a bundle of parallel microtubules: bi-directional motion caused by load-dependent polymerization and depolymerization. *J Stat Mech*, *2015*(1), 1008-1013. https://doi.org/10.1088/1742-5468/2015/01/P01008

Gildersleeve, R. F., Cross, A. R., Cullen, K. E., Fagen, A. P., & Williams, R. C. J. (1992). Microtubules grow and shorten at intrinsically variable rates. *J Biol Chem*, *267*(12), 7995-8006. https://www.jbc.org/article/S0021-9258(18)42399-X/pdf

Gonen, S., Akiyoshi, B., Iadanza, M. G., Shi, D., Duggan, N., Biggins, S., & Gonen, T. (2012). The structure of purified kinetochores reveals multiple microtubule-attachment sites. Nat Struct Mol Biol, 19(9), 925-929. https://doi.org/10.1038/nsmb.2358

Goshima, G., Wollman, R., Stuurman, N., Scholey, J. M., & Vale, R. D. (2005). Length control of the metaphase spindle. *Curr Biol*, *15*(22), 1979-1988. https://doi.org/10.1016/j.cub.2005.09.054
Holzbaur, E. L. F., & Goldman, Y. E. (2010). Coordination of molecular motors: from *in vitro* assays to intracellular dynamics. *Curr Opinion in Cell Biol*, *22*(1), 4-13. https://doi.org/10.1016/j.ceb.2009.12.014

Howard, J. (2001). *Mechanics of motor proteins and the cytoskeleton*. Sinauer Associates, Publishers.

Janson, M. E., de Dood, M. E., & Dogterom, M. (2003). Dynamic instability of microtubules is regulated by force. *J Cell Biol*, *161*(6), 1029-1034. https://doi.org/10.1083/jcb.200301147

Khodjakov, A., Cole, R. W., Bajer, A. S., & Rieder, C. L. (1996). The force for poleward chromosome motion in Haemanthus cells acts along the length of the chromosome during metaphase but only at the kinetochore during anaphase. *J Cell Biol*, *132*(6), 1093-1104. http://www.ncbi.nlm.nih.gov/pubmed/8601587

Khodjakov, A., & Rieder, C. L. (1996). Kinetochores moving away from their associated pole do not exert a significant pushing force on the chromosome. *J Cell Biol*, *135*(2), 315-327. http://www.ncbi.nlm.nih.gov/pubmed/8896591

Kiewisz, R., Fabig, G., Conway, W., Baum, D., Needleman, D., & Muller-Reichert, T. (2022). Three-dimensional structure of kinetochore-fibers in human mitotic spindles. *Elife*, *11*. https://doi.org/10.7554/eLife.75459

Kis, A., Kasas, S., Babic, B., Kulik, A. J., Benoit, W., Briggs, G. A., Schonenberger, C., Catsicas, S., & Forro, L. (2002). Nanomechanics of microtubules. *Phys Rev Lett*, *89*(24), 248101. https://doi.org/10.1103/PhysRevLett.89.248101

Klotz, J. H. (2006). *A Computational Approach to Statistics*. https://www.mimuw.edu.pl/~pokar/Statystykal/Literatura/KlotzBook.pdf

Laan, L., Husson, J., Munteanu, E. L., Kerssemakers, J. W. J., & Dogterom, M. (2008). Force-generation and dynamic instability of microtubule bundles. *105*(26), 8920-8925. https://doi.org/10.1073/pnas.0710311105

Maddox, P., Straight, A., Coughlin, P., Mitchison, T. J., & Salmon, E. D. (2003). Direct observation of microtubule dynamics at kinetochores in Xenopus extract spindles: implications for spindle mechanics. *J Cell Biol*, *162*(3), 377-382. https://doi.org/10.1083/jcb.200301088

Mahserejian, S. M., Scripture, J. P., Mauro, A. J., Lawrence, E. J., Jonasson, E. M., Murray, K. S., Li, J., Gardner, M., Alber, M., Zanic, M., & Goodson, H. V. (2022). Quantification of microtubule stutters: dynamic instability behaviors that are strongly associated with catastrophe. *MBoC*, *33*(3). https://doi.org/10.1091/mbc.E20-06-0348

Maiato, H., Fairley, E. A. L., Rieder, C. L., Swedlow, J. R., Sunkel, C. E., & Earnshaw, W. C. (2003). Human CLASP1 is an outer kinetochore component that regulates spindle microtubule dynamics. *Cell*, *113*(7), 891-904. https://doi.org/10.1016/S0092-8674(03)00465-3

Maiato, H., Rieder, C. L., Earnshaw, W. C., & Sunkel, C. E. (2003). How do kinetochores CLASP dynamic microtubules? *Cell Cycle*, *2*(6), 511-514. https://doi.org/10.4161/cc.2.6.576

McAinsh, A. D., & Meraldi, P. (2011). The CCAN complex: Linking centromere specification to control of kinetochore-microtubule dynamics. *Seminars in Cell & Dev Biol*, *22*(9), 946-952. https://doi.org/10.1016/j.semcdb.2011.09.016

McDonald, K. L., O'Toole, E. T., Mastronarde, D. N., & McIntosh, J. R. (1992). Kinetochore microtubules in PTK cells. *J Cell Biol*, *118*(2), 369-383. http://www.ncbi.nlm.nih.gov/pubmed/1629239

McIntosh, J. R., O'Toole, E., Morgan, G., Austin, J., Ulyanov, E., Ataullakhanov, F., & Gudimchuk, N. (2018). Microtubules grow by the addition of bent guanosine triphosphate tubulin to the tips of curved protofilaments [Article]. *Journal of Cell Biology*, *217*(8), 2691-2708. https://doi.org/10.1083/jcb.201802138

Miller, M. P., Asbury, C. L., & Biggins, S. (2016). A TOG Protein Confers Tension Sensitivity to Kinetochore-Microtubule Attachments. *Cell*, *165*(6), 1428-1439. https://doi.org/10.1016/j.cell.2016.04.030

Murray, L. E., Kim, H., Rice, L. M., & Asbury, C. L. (2022). Working strokes produced by curling protofilaments at disassembling microtubule tips can be biochemically tuned and vary with species. *Elife*, *11*. https://doi.org/10.7554/eLife.83225

Neahring, L., Cho, N. H., & Dumont, S. (2021). Opposing motors provide mechanical and functional robustness in the human spindle. *Dev Cell*, *56*(21), 3006-3018. https://doi.org/10.1016/j.devcel.2021.09.011

Nicklas, R. B. (1983). Measurements of the force produced by the mitotic spindle in anaphase. *J Cell Biol*, *97*(2), 542-548. http://www.ncbi.nlm.nih.gov/pubmed/6885908

Nicklas, R. B. (1988). The forces that move chromosomes in mitosis. *Annu Rev Biophys Biophys Chem*, *17*, 431-449. https://doi.org/10.1146/annurev.bb.17.060188.002243

O'Toole, E., Morphew, M., & McIntosh, J. R. (2020). Electron tomography reveals aspects of spindle structure important for mechanical stability at metaphase. *Molecular Biology of the Cell*, *31*(3), 184-195. https://doi.org/10.1091/mbc.E19-07-0405

Ou, G., & Scholey, J. M. (2022). Motor cooperation during mitosis and ciliogenesis. *Annu Rev Cell Dev Biol*, *38*(1), 49-74. https://doi.org/10.1146/annurev-cellbio-121420-100107

Pampaloni, F., Lattanzi, G., Jonas, A., Surrey, T., Frey, E., & Florin, E. L. (2006). Thermal fluctuations of grafted microtubules provide evidence of a length-dependent persistence length. *Proc Natl Acad Sci U S A*, *103*(27), 10248-10253. https://doi.org/10.1073/pnas.0603931103

Parmar, S., Gonzalez, S. J., Heckel, J. M., Mukherjee, S., McClellan, M., Clarke, D. J., Johansson, M., Tank, D., Geisness, A., Wood, D., & Gardner, M. (2023). Robust microtubule dynamics facilitate low tension kinetochore detachment in metaphase. J Cell Biol, 222(8). https://doi.org/10.1083/jcb.202202085

Poirier, M. G., Eroglu, S., & Marko, J. F. (2002). The bending rigidity of mitotic chromosomes. *MBoC*, *13*(6), 2170-2179. https://doi.org/10.1091/mbc.01-08-0401

Powers, A. F., Franck, A. D., Gestaut, D. R., Cooper, J., Gracyzk, B., Wei, R. R., Wordeman, L., Davis, T. N., & Asbury, C. L. (2009). The Ndc80 kinetochore complex forms load-bearing attachments to dynamic microtubule tips via biased diffusion. *Cell*, *136*(5), 865-875. https://doi.org/10.1016/j.cell.2008.12.045

Press, W. H., Flannery, B. P., Teukolsky, S. A., & Vetterling, W. T. *Numerical Recipes in C: The Art of Scientific Computing*.

Rai, A., Liu, T., Katrukha, E. A., Estevez-Gallego, J., Manka, S. W., Paterson, I., Diaz, J. F., Kapitein, L. C., Moores, C. A., & Akhmanova, A. (2021). Lattice defects induced by microtubule-stabilizing agents exert a long-range effect on microtubule growth by promoting catastophes. *PNAS*, *118*(51). https://doi.org/10.1073/pnas.2112261118

Renda, F., Magidson, V., Tikhonenko, I., Fisher, R., Miles, C., Mogilner, A., & Khodjakov, A. (2020). Effects of malleable kinetochore morphology on measurements of intrakinetochore tension. *Open Biol*, *10*(7). https://doi.org/10.1098/rsob.200101

Risteski, P., Jagric, M., Pavin, N., & Tolic, I. M. (2021). Biomechanics of chromosome alignment at the spindle midplane. *Curr Biol*, *31*(10), R574-R585. https://doi.org/10.1016/j.cub.2021.03.082

Rizk, R. S., Bohannon, K. P., Wetzel, L. A., Powers, J., Shaw, S. L., & Walczak, C. E. (2009). MCAK and paclitaxel have differential effects on spindle microtubule organization and dynamics. *MBoC*, *20*(6), 1639-1651. https://doi.org/10.1091/mbc.e08-09-0985

Rusan, N. M., Fagerstrom, C. J., Yvon, A. M., & Wadsworth, P. (2001). Cell cycle-dependent changes in microtubule dynamics in living cells expressing green fluorescent protein-alpha tubulin. Mol Biol Cell, 12(4), 971-980. http://www.ncbi.nlm.nih.gov/pubmed/11294900

Sanhaji, M., Friel, C. T., Wordeman, L., Louwen, F., & Yuan, J. (2011). Mitotic centromere-associated kinesin (MCAK): a potential cancer drug target. *Oncotarget*, *2*(12), 935-947. https://doi.org/10.18632/oncotarget.416

Sarangapani, K. K., Akiyoshi, B., Duggan, N. M., Biggins, S., & Asbury, C. L. (2013). Phosphoregulation promotes release of kinetochores from dynamic microtubules via multiple mechanisms. *Proc Natl Acad Sci U S A*, *110*(18), 7282-7287. https://doi.org/10.1073/pnas.1220700110

Schwietert, F., & Kierfeld, J. (2020). Bistability and oscillations in cooperative microtubule and kinetochore dynamics in the mitotic spindle. *New journal of physics*, *22*(5). https://doi.org/10.1088/1367-2630/ab7ede

Schwietert, F., Volkov, V. A., Pim J., H. V., Dogterom, M., Musacchio, A., & Kierfeld, J. (2022). Strain stiffening of Ndc80 complexes attached to microtubule plus ends. *Biophys J*, *121*(21), 4048-4062. https://doi.org/10.1016/j.bpj.2022.09.039

Skibbens, R. V., Rieder, C. L., & Salmon, E. D. (1995). Kinetochore motility after severing between sister centromeres using laser microsurgery: evidence that kinetochore directional instability and position is regulated by tension. *J Cell Sci*, *108 (Pt 7)*, 2537-2548. http://www.ncbi.nlm.nih.gov/pubmed/7593295

Skibbens, R. V., Skeen, V. P., & Salmon, E. D. (1993). Directional instability of kinetochore motility during chromosome congression and segregation in mitotic newt lung cells: a push-pull mechanism. *J Cell Biol*, *122*(4), 859-875. http://www.ncbi.nlm.nih.gov/pubmed/8349735

Sousa, A., Reis, R., Sampaio, P., & Sunkel, C. E. (2007). The *Drosophila* CLASP homologue, Mast/Orbit regulates the dynamic behaviour of interphase microtubules by promoting the pause state. *Cell Motility*, *64*(8), 605-620. https://doi.org/10.1002/cm.20208

Streitberg, B., & Rohmel, J. (1986). Exact distributions for permutations and rank tests: An introduction to some recently published algorithms. *Statistical Software Newsletter*, *12*, 10-17.

Stumpff, J., Ghule, P. N., Shimamura, A., Stein, J. L., & Greenblatt, M. (2014). Spindle microtubule dysfunction and cancer predisposition. *J Cell Phys*, *229*(12), 1881-1883. https://onlinelibrary.wiley.com/doi/abs/10.1002/jcp.24691

Stumpff, J., Wagenbach, M., Franck, A., Asbury, C. L., & Wordeman, L. (2012). Kif18A and chromokinesins confine centromere movements via microtubule growth suppression and spatial control of kinetochore tension. *Dev Cell*, *22*(5), 1017-1029. https://doi.org/10.1016/j.devcel.2012.02.013

Tien, J. F., Umbreit, N. T., Gestaut, D. R., Franck, A. D., Cooper, J., Wordeman, L., Gonen, T., Asbury, C. L., & Davis, T. N. (2010). Cooperation of the Dam1 and Ndc80 kinetochore complexes enhances microtubule coupling and is regulated by aurora B. *J Cell Biol*, *189*(4), 713-723. https://doi.org/10.1083/jcb.200910142

Tirnauer, J. S., Canman, J. C., Salmon, E. D., & Mitchison, T. J. (2002). EB1 targets to kinetochores with attached, polymerizing microtubules. *MBoC*, *13*(12), 4308-4316. https://doi.org/10.1091/mbc.E02-04-0236

VandenBeldt, K. J., Barnard, R. M., Hergert, P. J., Meng, X., Maiato, H., & McEwen, B. F. (2006). Kinetochores use a novel mechanism for coordinating the dynamics of individual microtubules. *Curr Biol*, *16*(12), 1217-1223. https://doi.org/10.1016/j.cub.2006.04.046

Varga, V., Helenius, J., Tanaka, K., Hyman, A. A., Tanaka, T. U., & Howard, J. (2006). Yeast kinesin-8 depolymerizes microtubules in a length-dependent manner. *Nat Cell Biol*, *8*(9), 957-962. http.://doi.org/10.1038/ncb1462

Volkov, V. A., Huis In 't Veld, P. J., Dogterom, M., & Musacchio, A. (2018). Multivalency of NDC80 in the outer kinetochore is essential to track shortening microtubules and generate forces. *Elife*, *7*. https://doi.org/10.7554/eLife.36764

Wan, X., Cimini, D., Cameron, L. A., & Salmon, E. D. (2012). The coupling between sister kinetochore directional instability and oscillations in centromere stretch in metaphase PtK1 cells. *Mol Biol Cell*, *23*(6), 1035-1046. https://doi.org/10.1091/mbc.E11-09-0767

Waters, J. C., Skibbens, R. V., & Salmon, E. D. (1996). Oscillating mitotic newt lung cell kinetochores are, on average, under tension and rarely push. *J Cell Sci*, *109 (Pt 12)*, 2823-2831. http://www.ncbi.nlm.nih.gov/pubmed/9013330

Wieczorek, M., Bechstedt, S., Chaaban, S., & Brouhard, G. (2015). Microtubule-associated proteins control the kinetics of microtubule nucleation. *Nat Cell Biol*, *17*(7), 907-916. https://doi.org/10.1038/ncb3188

Winey, M., Mamay, C. L., O'Toole, E. T., Mastronarde, D. N., Giddings, T. H., Jr., McDonald, K. L., & McIntosh, J. R. (1995). Three-dimensional ultrastructural analysis of the Saccharomyces cerevisiae mitotic spindle. J Cell Biol, 129(6), 1601-1615. http://www.ncbi.nlm.nih.gov/pubmed/7790357

Wordeman, L., Wagenbach, M., & von Dassow, G. (2007). MCAK facilitates chromosome movement by promoting kinetochore microtubule turnover. *J Cell Biol*, *179*(5), 869-879. https://doi.org/10.1083/jcb.200707120

Yamashita, N., Morita, M., Legant, W. R., Chen, B., Betzig, E., Yokota, H., & Mimori-Kiyousue, Y. (2015). Three-dimensional tracking of plus-tips by lattice light-sheet microscopy permits the quantification of microtubule growth trajectories within the mitotic apparatus. *J Biomedical Optics*, *20*(10), 101206-101206. https://doi.org/10.1117/1.jbo.20.10.101206

Zar, J. H. (1999). *Biostatistical analysis* (4th ed.). Prentice Hall.

Zelinski, B., & Kierfeld, J. (2013). Cooperative dynamics of microtubule ensembles: Polymerization forces and rescue-induced oscillations. *Phys Rev*, *87*(1). https://doi.org/10.1103/physreve.87.012703